

# High-pressure phase equilibria and element partitioning experiments on Apollo 15 green C picritic glass: Implications for the role of garnet in the deep lunar interior

David S. Draper<sup>a,\*</sup>, S. Andrew duFrane<sup>b</sup>, Charles K. Shearer Jr.<sup>a</sup>,  
Rachel E. Dwarzski<sup>a</sup>, Carl B. Agee<sup>a</sup>

<sup>a</sup> Institute of Meteoritics, 1 University of New Mexico, MSC03-2050, Albuquerque, NM 87131, USA

<sup>b</sup> Department of Earth and Planetary Sciences, 1 University of New Mexico, MSC03-2050, Albuquerque, NM 87131, USA

Received 26 April 2005; accepted in revised form 13 January 2006

## Abstract

We report results of nominally anhydrous near-liquidus experiments on a synthetic analog to very low-titanium Apollo 15 green C lunar picritic glass from ~2 to 5 GPa. Apollo 15 green C glass (A15C) is saturated with garnet and pyroxene on the liquidus at ~3 GPa. However, such an assemblage is unlikely to represent the lunar-mantle source region for this glass, and instead an olivine + orthopyroxene-dominated source is favored, in accord with earlier lower-pressure experiments on A15C. Near-liquidus garnet has a slight but significant majorite component at ~5 GPa in this iron-rich bulk composition, as expected from our previous work in ordinary-chondritic bulk compositions. Ion microprobe measurements of partitioning of Sr, Ba, Sc, Nd, Sm, Dy, Yb, Y, Zr, Hf, and Th between garnet and coexisting melt in these experiments are the first garnet partition coefficients (*D* values) available that are directly relevant to lunar compositions. *D* values for these garnets differ significantly compared to *D* values for garnets grown in more magnesian, terrestrial bulk compositions, which until now are all that have been available in modeling the possible role of garnet in the lunar interior. For example, *D* values for heavy rare earth elements are lower than are those from terrestrial basaltic systems. These partitioning values are well-described by the lattice-strain partitioning model, but predictive relationships for garnet partitioning using that model fail to match the measured values, as was the case in our earlier work on chondritic compositions. Using our new *D* values in place of the “terrestrial” values in a variety of models of lunar petrogenesis, we suggest that garnet is unlikely to be present in the source regions for very titanium-poor lunar liquids despite its appearance on the liquidus of A15C.

© 2006 Elsevier Inc. All rights reserved.

## 1. Introduction

Insights on petrogenetic processes occurring in the lunar interior have been gained from decades of study of samples returned by Apollo and Luna missions. These earlier studies have been augmented in recent years by increasing interest in lunar science prompted in part by results from robotic orbiters such as Lunar Prospector and Clementine, and by consortia such as the New Views of the Moon. Notwithstanding these intensive efforts, fundamental questions remain regarding the nature both of the source regions for

lunar magmas and of the pressure–temperature conditions over which melting took place that gave rise to them, e.g., Shearer and Papike (1999) and Hess (2000).

Lunar picritic glasses are thought to be the result of fire-fountain eruptions on the Moon, more or less during the period of peak lunar magmatism (Papike et al., 1998). Their compositions span the range of nearly all lunar basalts. As probes of the lunar interior, picrite glasses are unique in that they are quenched near-primary liquids that originated at greater depths in the Moon compared to dominantly crystalline mare basalts. Picrite glass compositions range from a very low-Ti end member having ~48 wt% SiO<sub>2</sub>, <0.5 wt% TiO<sub>2</sub>, Mg# (molar ratio of Mg/(Mg + Fe)) ~65, and CaO/Al<sub>2</sub>O<sub>3</sub> ~ 1.1 to a very high-Ti

\* Corresponding author. Fax: +1 505 277 8803.

E-mail address: [david@draper.name](mailto:david@draper.name) (D.S. Draper).

endmember having ~34 wt% SiO<sub>2</sub>, ~16 wt% TiO<sub>2</sub>, Mg# ~50, and CaO/Al<sub>2</sub>O<sub>3</sub> ~ 1.35 (Delano, 1986). Along with lunar mare basalt compositions, the glasses were extensively studied experimentally (largely during the 1970s) in applications of the inverse experimental approach, i.e., mapping liquidus mineralogy as a function of pressure (Basaltic Volcanism Study Project, 1981), in order to constrain their depths of origin (Longhi, 1992a). Most of these picrite glass studies, summarized below, found points of near-liquidus multiple saturation in the pressure range 1.5–2.5 GPa, and these findings have contributed to the variety of interpretations for lunar magmagenesis, e.g., extents of magma ocean processing, role of cumulate overturn, degree of source region refertilization by Ti- and incompatible-rich materials such as KREEP (K-, rare earth element-, and P-rich component), and the role of assimilation (Delano, 1986; Longhi, 1992b; Hess and Parmentier, 1995; Shearer and Papike, 1999; Hess, 2000).

Most of the pre-1990s studies of mare basalts concluded that garnet was not in their mantle sources. This conclusion was based on (1) the assumption that mare magmatism represented melting in the shallow lunar mantle outside the stability field of garnet, (2) the observation that the trace element data for the mare basalts did not exhibit typical “garnet signature” trace-element fractionations, and (3) the prediction from lunar magma ocean models that the source region of the mare basalts were essentially low-Al cumulates. In ensuing years, reinterpretation of experimental studies on the lunar pyroclastic glasses by Delano (1986) and Longhi (1992b) expanded the mantle pressure regimes over which mare magmatism may have occurred (~1000 km). More recent trace element and isotopic data (see below) have been interpreted as indicating the presence of garnet in the source regions for some of the mare basaltic magmas represented by the pyroclastic glasses. These recent data present a dilemma for mare magmatism because sources for these magmas are still thought to be Al-poor (Longhi, 1995) and the stability of garnet as a liquidus or near-liquidus phase for picrite glasses has not been documented.

Because essentially all experimental studies on picrite glasses performed to date were carried out at pressures lower than those at which garnet is likely to become stable in these bulk compositions, phase equilibrium evidence relevant to this question is scant. We have begun to redress that lack by performing near-liquidus inverse-approach experiments on several lunar picrite glass compositions at garnet-relevant pressures in order to constrain that mineral's possible role in their source regions. The experiments are intended both to identify the high-pressure liquidus mineralogy of a range of picrite glass compositions and to measure trace element partitioning between those liquidus minerals and coexisting picrite melts. Garnet-liquid trace element partition coefficients that have been used to evaluate the role of garnet in lunar magmagenesis have heretofore, by necessity, come from experimental studies on terrestrial compositions, which are substantially more magnesian than are lunar compositions. As we will show

below and as indicated by previous determinations of garnet-liquid partitioning in Fe-rich chondritic liquids (Draper et al., 2003), partition coefficients for some important elements change markedly in such Fe-rich systems.

In this contribution, we report results of high pressure experiments on Apollo 15 green C glass (A15C hereafter), the picrite glass poorest in TiO<sub>2</sub>. These experiments document both anhydrous high-pressure near-liquidus phase relations of this composition and determine trace element partitioning between low-Ti lunar liquids and coexisting near-liquidus garnet using secondary ion mass spectrometry (SIMS, or ion microprobe). Understanding the constraints on the presence or absence of this mineral has important implications for the physical and chemical structure of the lunar interior.

In the following sections, we review previous experimental work on lunar basaltic compositions and the more recent geochemical evidence pointing to a possible role of garnet in their source regions. We then outline our experimental and analytical approach before reporting the results of our experiments and the applications of these results to constraining the nature of the deep lunar mantle.

### 1.1. Review of previous experimental work

Papike et al. (1998) summarized experimental studies performed on both mare basalt and picrite glass compositions at pressures from ~1.0 to 2.5 GPa. These include Walker et al. (1972, 1975, 1976, 1977); Green et al. (1971a,b, 1975); Kushiro et al. (1972); Hodges and Kushiro (1974); Chen et al. (1982); Chen and Lindsley (1983); Kesson (1975); Grove and Vaniman (1978); O'Hara et al. (1970); Ringwood and Essene (1970); Delano (1980); Longhi (1992b,a, 1995); and Longhi et al. (1974). More recent work includes experiments by Wagner and Grove (1997), Elkins-Tanton et al. (2000; 2003), and Van Orman and Grove (2000). Most of these studies showed, in general, that multiple saturation pressures for the picrite glasses were greater than were those for mare basalts (2.0–2.5 GPa for most glasses compared to 0.5–1.5 GPa for most mare basalts). In addition, the saturating assemblage was olivine + low-Ca pyroxene ± spinel for a wide variety of lunar compositions. These include the low-Ti picrite glasses studied by Chen et al. (1982), Chen and Lindsley (1983), and Grove and Vaniman (1978); for the high-Ti glass compositions studied by Wagner and Grove (1997); Delano (1980); and Walker et al. (1975); and for the low-Ti mare basalts studied by Ringwood and Essene (1970). In contrast, almost all the high-Ti crystalline mare basalt compositions studied experimentally were saturated with olivine + clinopyroxene + a Ti-rich phase such as ilmenite (Ringwood and Essene, 1970; Longhi et al., 1974; Green et al., 1975; Kesson, 1975).

There are a variety of interpretations for these results. Source regions for lunar mare basalts could simply be different from those for the picrite glasses; their differing multiple-saturation assemblages and pressures would correspond to the different lithologies of their respective

sources and/or the differing pressures at which melting occurred. Alternatively, the multiple-saturation pressures shown by these compositions could be averages of a set of polybaric processes, as argued by Longhi (1992b). In this view, multiple saturation pressures for the mare basalts (assuming they represent liquid compositions) could represent minimum depths of melting, such that the actual depths were similar to those for the picrite glasses. A lower apparent saturation depth for crystalline mare basalts could result, for example, from extensive olivine fractionation from a picritic magma parental to both the mare basalts and picrite glasses. Papike et al. (1998) favored this latter interpretation, although they did not directly address the implications of the different saturating assemblages between the high-Ti basalts and the other three sample types.

The existence of a low-pressure multiple-saturation point does not by any means preclude the existence of additional points at other pressures. Therefore, it is quite possible that picrite glasses could show additional points of multiple saturation, perhaps with garnet as part of the saturating assemblage, at pressures above those shown in the studies cited above. The results reported here constitute the first phase equilibrium data on picritic glasses at pressures above  $\sim 2.3$  GPa, allowing this notion to be directly tested.

### 1.2. Geochemical evidence for garnet

Geophysical evidence for garnet is ambiguous largely because data from Apollo-deployed seismometers are of insufficient resolution (Khan et al., 2000; Lognonne et al., 2003). Geochemical evidence for garnet in lunar magma sources is recent compared to most of the huge amount of lunar research that began before the end of the Apollo program, and includes isotopic (Beard et al., 1998) and trace element (Neal, 2001; Neal and Shearer, 2004) data. Beard et al. (1998) measured Lu–Hf isotopic systematics in crystalline mare basalts and argued that fractionations of Lu/Hf and Sm/Nd in low-Ti magmas may have been produced by garnet and orthopyroxene in the sources, although garnet was thought to have been consumed during polybaric melting that began in the garnet stability field. However, as shown by Neal (2001), such a signature does not extend to other trace elements in mare basalts, such as Y, Yb, Zr, and Sc. Neal (2001) illustrated, for certain lunar picrite glasses, a clear signature of garnet retention in the source (e.g., Zr/Y and chondrite-normalized Sm/Yb above those for KREEP while having low Sc/Sm), and agreed that if garnet was present at some point in mare basalt sources, it was consumed by comparatively high degrees of partial melting to generate those basalts.

Neal (2001) further argued that only a garnet-bearing source rock could produce melts having both lower Sc/Sm than the source and higher chondrite-normalized Sm/Yb, assuming the bulk Moon composition of Taylor (1982, 1992), and that this garnet-bearing source represents a remnant of “primitive Moon” that did not take part in the wholesale melting that produced the early lunar magma

ocean. The logical extension of this conclusion is that not all crystalline mare basalts and picrite glasses originated from similar sources. The glasses cited by Neal (2001) that have the required compositional features outlined above are Apollo 12 red, Apollo 14 green A and yellow, Apollo 17 type I, and Apollo 17 74220-type. Additional analysis by Neal and Shearer (2004) focused on the comparatively Ti-rich glasses Apollo 14 orange and black and Apollo 12 red as the most likely candidates for garnet in the source, accounting for Apollo 14 green A via the involvement of KREEP.

In contrast to the reasoning of Neal (2001) and Neal and Shearer (2004), Longhi (1995) has argued that garnet is unlikely to be a residual phase for melting that produced mare basalts and picrite glasses. His polybaric melting models predict that source regions for these magmas would be too poor in Al for an aluminous phase to be stable. Our experimental program should be able to help resolve this apparent conflict, both from the perspective of high-pressure phase relations and trace element partitioning. Our first step is to examine the A15C composition. Although this glass is not included in the candidate group defined by Neal (2001), it remains of interest because it constitutes one endmember of the lunar picrite glass suite (e.g., highest SiO<sub>2</sub> and Mg#, lowest TiO<sub>2</sub> and CaO/Al<sub>2</sub>O<sub>3</sub>). In addition, its lower-pressure phase relations are already well-known from the work of Elkins-Tanton et al. (2003). Our preliminary results were reported in abstract form (Shearer et al., 2003; Draper et al., 2004) and are fully documented here.

## 2. Experimental and analytical procedures

### 2.1. Experimental

#### 2.1.1. Starting material

Experiments were performed on a synthetic powdered glass with a bulk composition (Table 1) very close to that of A15C as reported by Delano (1986). This powder was synthesized by L. Elkins-Tanton for her study of green glass phase relations (Elkins-Tanton et al., 2003) and kindly provided for our use in this study. Because our experiments were performed on the exact same powder used in that study, there are no discrepancies between the two sets of results that might occur from slight differences in starting material bulk composition.

In order to measure trace element partitioning, we doped the A15C powder (for experiments beginning with run A67 and higher numbers; those with lower numbers were undoped) with a “cocktail” of nitric and hydrofluoric acids in which were dissolved reagent-grade solutions of Sr, Ba, Sc, Nd, Sm, Dy, Yb, Y, Zr, Hf, and Th. These elements were doped at  $\sim 50$ – $300$  times chondritic abundance levels so that good-quality SIMS data would be straightforward to obtain. The particular elements were chosen for two reasons: first, to eliminate isobaric interferences during SIMS analysis; and second, to allow meaningful application of the lattice-strain model for trace element partitioning

Table 1  
Composition of starting material

Oxide	1	2	Trace elements (ppm)	
SiO <sub>2</sub>	48.3	48.0	Sc	763 (13)
TiO <sub>2</sub>	0.23	0.26	Sr	54.3 (8.6)
Al <sub>2</sub> O <sub>3</sub>	7.77	7.74	Y	232 (17)
FeO	16.12	16.50	Zr	688 (6)
MnO	0.19	0.19	Ba	423 (46)
MgO	18.27	18.20	Nd	17.6 (1.9)
CaO	8.59	8.57	Sm	25.3 (2.9)
Na <sub>2</sub> O	0.00	0.00	Dy	21.8 (1.9)
Cr <sub>2</sub> O <sub>3</sub>	0.55	0.57	Yb	16.4 (1.7)
Total	100.01	100.03	Hf	37.4 (4.5)
			Th	1.24 (0.07)
Mg#	66.9	66.3		
CaO/Al <sub>2</sub> O <sub>3</sub>	1.11	1.11		

1, composition of starting glass from Elkins-Tanton et al. (2003).

2, composition of Apollo 15 green C from Delano (1986).

Trace element composition is average of 3 ion microprobe analyses, 1 –  $\sigma$  standard deviations in parentheses.

Mg# = molar Mg/Mg + Fe  $\times$  100.

promulgated by Blundy and Wood (1994) for clinopyroxene and applied in recent years to garnets relevant to terrestrial (van Westrenen et al., 2001b) and martian (Draper et al., 2003) bulk compositions. Another purpose of our high-pressure work on lunar picrite glasses is to isolate important crystal-chemical factors controlling garnet-melt trace element partitioning (e.g., effects of Fe, Ti, Cr, and majorite), and these applications will be developed in future contributions.

### 2.1.2. Run conditions

Run conditions and resulting phase assemblages are listed in Table 2. Experiments at 2.5 Pa and above were run under nominally anhydrous conditions in a Walker-type multianvil press at the Institute of Meteoritics, University of New Mexico, using cell assemblies, procedures, and calibrations identical to those described by Agee et al. (1995), where complete details can be found. Tungsten carbide cubes with corners truncated to an 8 mm edge length were used with cast, finned octahedra of Aremco Ceramacast© 584 ceramic. These octahedra were fired at 1100 °C prior to being drilled out for assembly fabrication, and stored in a drying oven at ~110 °C until ready for use. The powdered starting material, also stored in the drying oven between experiments, was placed inside graphite capsules with press-fit lids and insulated from the rhenium foil heater walls by hard-fired alumina sheaths. We positioned samples in the center of the heater and bracketed the sample capsules with crushable alumina spacers. Temperatures were measured by radially-inserted W/Re thermocouples, with the junction near the capsule at the center of the heater, and controlled by a Eurotherm 930P programmable controller. Pressures were applied at 3–5 GPa/h. Runs DD504-6 and DD504-2, at 1.8 GPa, were conducted using a 1/2-in., endloaded piston-cylinder at the University of Oregon. These two reconnaissance experiments were run

Table 2  
Run conditions for experiments on Apollo 15 green C

Run	<i>P</i> (GPa)	<i>T</i> (°C)	Duration (min)	Assemblage
DD504-6	1.8	1625	180	Liq(100)
DD504-2	1.8	1590	120	Liq(100)
A83	3.0	1800	109	Liq(100)
A81	3.0	1750	35	Liq(100)
A107	3.0	1725 <sup>a</sup>	90	Liq(90), px(10)
A8	3.0	1700	390	Liq(53), px(47)
A41	3.0	1675	68	Liq(13), px(63), gt(24)
A87	3.5	1825	95	Liq(100)
A67	3.5	1775	141	Liq(98), gt(2)
A42	3.5	1750	120	Liq(64), px(32), gt(4)
A38	3.5	1725	120	Liq(29), px(57), gt(14)
A57	4.0	1800 <sup>b</sup>	43	Liq(82), px(11), gt(9)
A138	4.0	1600	30	Liq(89), px(10), gt(1)
A140	4.5	1600	30	Liq(83), px(10), gt(7)
A218	5.0	1800	61	Liq(100)
A221	5.0	1650	62	Liq(89), px(5), gt(6)
A228	5.0	1625	60	Liq(87), gt(13) <sup>c</sup>
A229	7.0	1775	59	Liq(89), gt(11)
A225	7.0	1725	60	Liq(73), gt(18)

Values in parentheses are weight percent modes calculated by least-squares mass balance.

<sup>a</sup> Intended *T* for this run was 1775 °C; phase assemblage and compositions (Table 3) reflect lower temperature, probably owing to problem of capsule placement in heater. Reported *T* is estimate consistent with other results.

<sup>b</sup> This run's temperature fell to ~1000 °C after 20 min at target conditions; it was returned to target *T* but then suffered a furnace failure after another 15 min during which *T* was much less stable than in other runs. Thus, the temperature reflected by the assemblage and mode in this run is likely substantially less than 1800 °C. This is denoted by a downward arrow on this run's symbol in Fig. 2.

<sup>c</sup> Run A228 was likely slightly higher *T* than Run 221; Mg# of melt is 66 vs. 63 for A221 (see Table 3).

in talc-pyrex cells. Temperatures were monitored using W5Re-W26Re thermocouples and controlled with an Omega electronic ice point and a Eurotherm Model 808 digital temperature controller. We applied no pressure correction to thermocouple emf. Reported pressures are nominal (Heise gauge) and incorporate ~10% correction for friction. The samples were quenched in 1–2 s by cutting power to the graphite furnace tubes.

Most experiments were held at target conditions for 30–120 min. Multianvil and piston-cylinder runs were quenched by cutting power to the heater, which caused temperatures to fall below the glass transition in  $\leq 10$  s and to room temperature in less than 5 min. Successful run products were mounted in epoxy, ground flat, and polished for electron microprobe and SIMS analyses.

### 2.1.3. Approach to equilibrium

Achieving chemical equilibrium in multianvil experimentation is more difficult than it is in other forms of experiments (e.g., piston-cylinder runs), due in large part to the strong thermal gradients that are unavoidable in multianvil runs. Vagaries in the precise placement of the thermocouple junction with respect to the sample, and potential displacements of the sample capsule from the

heater's midsection, aggravate the difficulty. Although we do not claim to have achieved perfect equilibrium in these experiments, the following considerations give us confidence that our results are acceptable.

First, in all subliquidus experiments reported here, garnet and pyroxene grains grew to relatively large sizes (50–400  $\mu\text{m}$  in longest dimension) with well-formed faces, in the region closest to the assembly's "hot zone" (see Fig. 1 for an example). Mineral compositions are reasonably homogeneous, as shown both by standard deviations on electron probe microanalyses (Table 3) and by backscattered electron images with fairly uniform grey levels, like those in Fig. 1. Appreciable zoning occurs only in thin (a few  $\mu\text{m}$ ) rinds that we infer to have formed during quenching, and these rinds were avoided during electron and ion microprobe analysis. Second, quench melt compositions also display reasonable homogeneity (Table 3) given that the melt in all experiments quenched to an intergrown mass

of microlites rather than to a glass (Fig. 1), although these analyses are less homogeneous than are those of crystalline phases. In addition, this felty texture resulted in electron microprobe totals of 95–98% in some experiments, a situation not uncommon in multianvil work on ultramafic compositions.

## 2.2. Analytical

### 2.2.1. Electron microprobe conditions

Polished run products were analyzed for major elements using the JEOL 8200 Superprobe in the Institute of Meteoritics operating at 15 keV accelerating potential and using standards of natural and synthetic minerals and glasses. Mineral phases were analyzed with a focused, 1- $\mu\text{m}$  beam and microcrystalline quenched melt was analyzed with a defocused beam 20–30  $\mu\text{m}$  in diameter. Major elements were counted for 20 s on peak and 10 s on background, and minor elements for 30 s on peak and 15 s on background. All electron microprobe data were obtained with a 20-nA beam current. Because this bulk composition is nominally alkali-free, we did not operate at low beam current for analyses of quenched melt as we customarily do when alkalis are present. Major element compositions reported below are averages of 5–20 spots on each phase in each run product.

### 2.2.2. Ion microprobe conditions

After electron microprobe analysis, carbon coats were removed from run products and then gold-coated for SIMS analysis. Analyses were made using primary  $\text{O}^-$  ions accelerated through a nominal potential of 10.0 kV. A primary beam current of 20 nA was focused on the sample over a spot diameter of 20  $\mu\text{m}$ . Sputtered secondary ions were energy filtered using a sample offset voltage of 105 V and an energy window of  $\pm 25$  V. Analyses involved repeated cycles of peak counting. The analytical procedure included counting on a background position to monitor detection noise. Absolute concentrations of each element were calculated using empirical relationships, derived from daily calibrations, of the measured ratios of trace element ions to  $^{30}\text{Si}^+$  ions (normalized to known  $\text{SiO}_2$  content) to element concentrations. Calibration curves were constructed using two or three glass standards for each element. Calibration curves for each element have correlation coefficients of greater than 0.97. Analytical precision is addressed in Table 4 by comparison between the nominal composition of one of our glass standards and its composition when measured as an unknown using our calibrations. These compare very well with the exception of Th, for which the nominal composition was 1.1 ppm but which we measured at 3.1 ppm. In any case,  $D$  values listed are ratios of Si-normalized intensity ratios, to avoid propagation of any uncertainty arising from applying calibration curves.

We examined our SIMS analyses in detail to investigate the possibility that patches of melt may have been

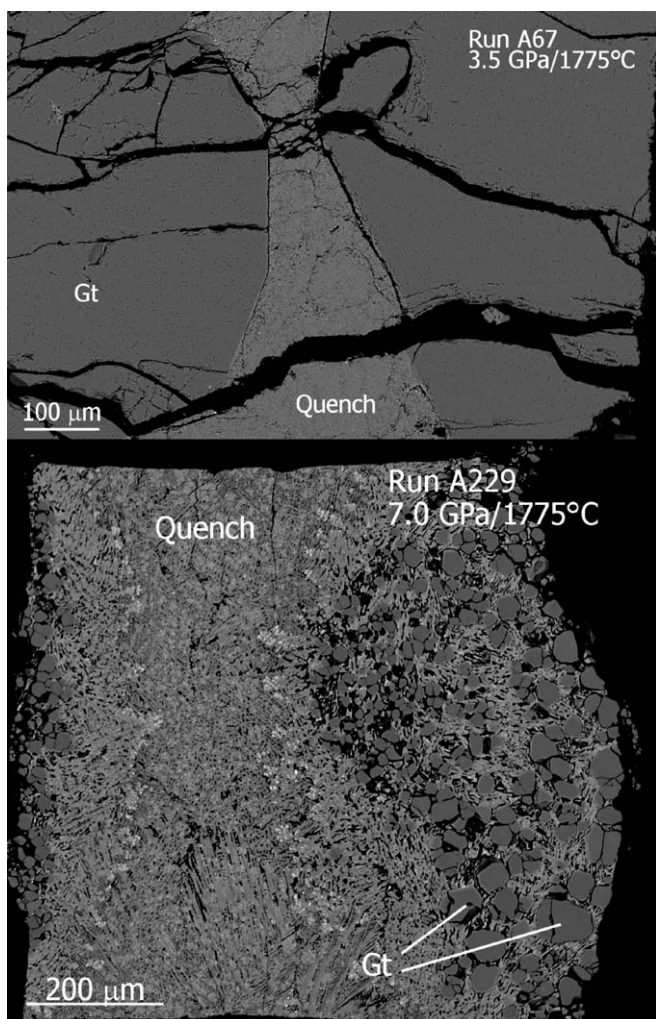


Fig. 1. Backscattered electron photomicrographs of run products. Gt, garnet; Quench, quenched melt. Top, run A67 with large garnet grains. Large black voids are decompression fractures. Bottom, run A229 with smaller garnet grains.

Table 3  
Electron microprobe analyses of subliquidus run products

	Run A107		Run A8		Run A41			Run A67	
	Quench	Pyx	Quench	Pyx	Quench	Gar	Pyx	Quench	Gar
SiO <sub>2</sub>	45.1 (1.0)	48.3 (0.7)	42.8 (1.5)	51.5 (0.9)	45.3 (1.1)	41.8 (0.3)	53.2 (0.5)	45.3 (0.9)	42.6 (0.2)
TiO <sub>2</sub>	0.22 (0.02)	0.21 (0.03)	0.57 (0.17)	0.03 (0.02)	0.73 (0.12)	0.22 (0.08)	0.03 (0.03)	0.24 (0.04)	0.05 (0.02)
Al <sub>2</sub> O <sub>3</sub>	10.22 (0.17)	10.73 (0.15)	10.29 (0.43)	5.44 (0.31)	6.37 (0.13)	21.35 (0.47)	3.19 (0.99)	7.92 (0.17)	21.82 (0.25)
FeO	15.23 (0.13)	14.50 (0.06)	22.77 (1.52)	11.13 (0.11)	26.79 (1.40)	15.63 (0.44)	14.34 (0.35)	15.36 (0.22)	10.13 (0.25)
MnO	0.20 (0.02)	0.17 (0.01)	0.22 (0.03)	0.19 (0.02)	0.22 (0.01)	0.26 (0.01)	0.18 (0.01)	0.17 (0.01)	0.20 (0.03)
MgO	17.06 (0.40)	17.21 (0.31)	14.47 (0.54)	23.61 (0.32)	11.74 (0.40)	15.88 (0.36)	20.41 (0.32)	15.99 (0.17)	21.18 (0.17)
CaO	7.95 (0.14)	7.82 (0.05)	9.10 (0.36)	7.52 (0.21)	9.90 (0.20)	5.89 (0.35)	9.92 (0.57)	9.16 (0.40)	3.87 (0.07)
Na <sub>2</sub> O	0.17 (0.04)	0.17 (0.03)	0.06 (0.02)	0.03 (0.01)	0.02 (0.02)	b.d.l.	0.03 (0.01)	0.47 (0.03)	b.d.l.
Cr <sub>2</sub> O <sub>3</sub>	0.55 (0.04)	0.53 (0.01)	0.46 (0.03)	0.61 (0.03)	0.19 (0.03)	1.28 (0.12)	0.28 (0.10)	0.24 (0.02)	1.52 (0.24)
Total	96.78 (1.31)	99.73 (1.14)	100.73 (0.62)	100.10 (0.81)	101.30 (0.15)	102.26 (0.41)	101.54 (0.28)	94.96 (0.71)	101.42 (0.13)
Mg#	66.6	68.0	53.2	79.1	43.9	55.7	65.3	65.0	78.8
	Run A42		Run A38			Run A57			
	Quench	Gar	Pyx	Quench	Gar	Pyx	Quench	Gar	Pyx
SiO <sub>2</sub>	47.6 (0.2)	40.0 (0.3)	49.7 (0.6)	41.9 (0.9)	38.9 (0.4)	49.7 (0.5)	44.8 (2.3)	42.6 (0.1)	56.5 (0.4)
TiO <sub>2</sub>	0.33 (0.05)	0.12 (0.02)	0.02 (0.02)	0.53 (0.03)	0.15 (0.04)	0.03 (0.02)	0.27 (0.08)	0.04 (0.02)	0.02 (0.02)
Al <sub>2</sub> O <sub>3</sub>	8.65 (0.05)	22.01 (0.37)	4.01 (1.01)	7.39 (0.16)	21.72 (0.23)	4.01 (0.32)	6.56 (0.74)	21.35 (0.09)	1.43 (0.06)
FeO	19.74 (0.45)	11.92 (0.16)	10.60 (0.64)	24.07 (0.20)	13.67 (0.36)	12.66 (0.21)	16.54 (0.90)	12.75 (0.20)	12.21 (0.21)
MnO	0.22 (0.03)	0.23 (0.03)	0.19 (0.04)	0.23 (0.02)	0.24 (0.02)	0.18 (0.02)	0.19 (0.02)	0.25 (0.01)	0.15 (0.01)
MgO	15.01 (0.26)	18.91 (0.25)	25.76 (2.31)	12.71 (0.15)	17.50 (0.33)	22.26 (0.25)	15.68 (1.22)	19.06 (0.26)	29.22 (0.16)
CaO	9.80 (0.08)	5.29 (0.34)	6.51 (1.45)	10.17 (0.11)	5.58 (0.33)	8.73 (0.27)	9.52 (0.95)	4.36 (0.11)	2.09 (0.20)
Na <sub>2</sub> O	0.04 (0.02)	b.d.l.	0.02 (0.01)	0.03 (0.02)	b.d.l.	0.02 (0.01)	0.03 (0.02)	b.d.l.	b.d.l.
Cr <sub>2</sub> O <sub>3</sub>	0.44 (0.03)	2.01 (0.06)	0.59 (0.10)	0.23 (0.02)	1.54 (0.13)	0.41 (0.05)	0.36 (0.06)	1.80 (0.07)	0.25 (0.03)
Total	101.80 (0.17)	100.54 (0.30)	97.41 (0.84)	97.28 (0.80)	99.35 (0.51)	98.00 (0.37)	93.96 (1.94)	102.24 (0.21)	101.85 (0.38)
Mg#	57.6	73.9	81.1	48.5	69.5	75.8	62.7	72.7	81.0
	Run A138		Run A140			Run A221			
	Quench	Gar	Pyx	Quench	Gar	Pyx	Quench	Gar	Pyx
SiO <sub>2</sub>	44.6 (1.1)	39.4 (0.4)	51.6 (0.4)	44.0 (2.1)	40.9 (0.5)	54.2 (0.2)	46.9 (0.6)	42.9 (0.3)	56.0 (0.4)
TiO <sub>2</sub>	0.25 (0.03)	0.10 (0.02)	b.d.l.	0.25 (0.08)	0.05 (0.04)	b.d.l.	0.26 (0.03)	0.04 (0.03)	b.d.l.
Al <sub>2</sub> O <sub>3</sub>	8.19 (0.39)	20.82 (0.13)	3.28 (0.25)	6.83 (0.53)	21.32 (0.14)	2.18 (0.06)	6.91 (0.37)	20.95 (0.21)	1.93 (0.11)
FeO	16.59 (0.50)	11.13 (0.08)	10.61 (0.22)	16.46 (1.00)	11.55 (0.50)	11.08 (0.04)	16.43 (0.23)	10.46 (0.11)	10.00 (0.12)
MnO	0.20 (0.02)	0.26 (0.01)	0.15 (0.03)	0.21 (0.03)	0.25 (0.02)	0.15 (0.01)	0.20 (0.02)	0.21 (0.02)	0.13 (0.02)
MgO	15.79 (0.68)	18.39 (0.09)	28.75 (0.22)	14.85 (1.29)	18.70 (0.77)	29.36 (0.12)	16.32 (0.24)	20.44 (0.30)	30.05 (0.24)
CaO	8.90 (0.26)	5.18 (0.11)	2.09 (0.16)	9.22 (0.62)	4.60 (0.41)	1.97 (0.02)	8.33 (0.17)	3.79 (0.29)	1.97 (0.17)
Na <sub>2</sub> O	0.02 (0.01)	b.d.l.	b.d.l.	0.03 (0.02)	b.d.l.	b.d.l.	0.03 (0.02)	b.d.l.	b.d.l.
Cr <sub>2</sub> O <sub>3</sub>	0.44 (0.04)	2.83 (0.06)	0.63 (0.05)	0.29 (0.04)	2.55 (0.29)	0.36 (0.03)	0.33 (0.02)	2.25 (0.14)	0.35 (0.04)
Total	94.99 (1.02)	98.08 (0.46)	97.09 (0.33)	92.15 (2.56)	99.95 (0.46)	99.37 (0.24)	95.73 (0.64)	101.03 (0.34)	100.47 (0.35)
Mg#	62.9	74.7	82.8	61.6	74.3	82.5	63.9	77.7	84.3
	Run A228		Run A229		Run A225				
	Quench	Gar	Quench	Gar	Quench	Gar			
SiO <sub>2</sub>	49.4 (1.8)	42.5 (0.5)	48.9 (1.1)	43.0 (1.1)	48.6 (2.2)	43.7 (0.7)			
TiO <sub>2</sub>	0.13 (0.06)	0.05 (0.03)	0.12 (0.09)	0.04 (0.03)	0.15 (0.24)	0.06 (0.03)			
Al <sub>2</sub> O <sub>3</sub>	5.35 (0.57)	21.85 (0.75)	5.26 (1.26)	20.28 (0.48)	2.62 (1.10)	19.17 (0.98)			
FeO	16.11 (2.14)	11.85 (0.53)	14.37 (1.62)	10.87 (0.16)	16.54 (1.46)	12.21 (0.15)			
MnO	0.20 (0.03)	0.22 (0.01)	0.19 (0.02)	0.21 (0.01)	0.20 (0.02)	0.22 (0.02)			
MgO	17.65 (1.39)	19.20 (1.02)	19.40 (0.83)	21.15 (0.37)	17.76 (1.85)	20.25 (0.60)			
CaO	8.51 (0.69)	4.43 (0.64)	7.89 (0.32)	3.76 (0.24)	9.03 (0.54)	4.35 (0.27)			
Na <sub>2</sub> O	0.03 (0.02)	b.d.l.	0.03 (0.02)	b.d.l.	0.05 (0.02)	b.d.l.			
Cr <sub>2</sub> O <sub>3</sub>	0.28 (0.05)	1.41 (0.72)	0.44 (0.03)	1.54 (0.07)	0.22 (0.05)	1.42 (0.04)			
Total	97.66 (1.12)	101.53 (0.47)	96.62 (1.55)	100.86 (1.32)	95.19 (2.22)	101.39 (0.58)			
Mg#	66.1	74.3	70.6	77.6	65.7	74.7			

Values are averages of 5–10 spots per phase. Values in parentheses are 1 –  $\sigma$  standard deviations. *Quench*, quenched melt; *Pyx*, pyroxene; *Gar*, garnet; and b.d.l., below detection limits.

Table 4  
Partition coefficients calculated from ratios of Si-normalized SIMS intensities

	A67	A138	A140	A228	A229	AH83-KL2	
						Meas.	Std.
Sc	2.45 (0.13)	1.80 (0.10)	2.49 (0.19)	1.61 (0.15)	1.27 (0.19)	31.8	32.0
Sr	0.002 (0.001)	0.18 (0.11)	0.11 (0.05)	0.080 (0.014)	0.052 (0.014)	321	380
Y	1.06 (0.07)	1.16 (0.16)	1.28 (0.16)	0.84 (0.13)	0.52 (0.09)	25.2	26.0
Zr	0.17 (0.02)	0.40 (0.10)	0.34 (0.04)	0.25 (0.05)	0.089 (0.032)	162	160
Ba	0.001 (0.001)	0.032 (0.019)	0.047 (0.023)	0.050 (0.014)	0.088 (0.045)	129	130
Nd	0.033 (0.013)	0.22 (0.08)	0.19 (0.08)	0.14 (0.04)	0.099 (0.041)	22.1	22.0
Sm	0.14 (0.07)	0.40 (0.15)	0.23 (0.12)	0.25 (0.10)	0.19 (0.13)	5.2	5.7
Dy	0.66 (0.14)	0.89 (0.21)	0.83 (0.21)	0.60 (0.14)	0.36 (0.11)	4.6	5.4
Yb	2.11 (0.44)	1.86 (0.42)	2.41 (0.60)	1.50 (0.32)	1.06 (0.42)	2.3	2.1
Hf	0.25 (0.10)	0.51 (0.22)	0.31 (0.13)	0.39 (0.16)	0.19 (0.18)	4.3	4.4
Th	0.065 (0.051)	0.21 (0.12)	0.28 (0.15)	0.22 (0.12)	0.18 (0.14)	3.1	1.1
E (GPa)	550 (36)	280 (38)	369 (75)	274 (58)	226 (72)		
$D_0$	3.19 (0.25)	2.10 (0.18)	2.95 (0.50)	1.78 (0.24)	1.33 (0.27)		
$r_0$ (Å)	0.919 (0.006)	0.919 (0.012)	0.912 (0.018)	0.904 (0.021)	0.882 (0.037)		
$r^2$	0.997	0.987	0.976	0.978	0.967		
<i>Refits to Eq. (1) omitting <math>D_{Nd}, D_{Sm}</math> (see text)</i>							
E (GPa)	684 (36)	182 (55)	704 (175)	608 (117)	689 (112)		
$D_0$	3.59 (0.74)	1.69 (0.15)	3.99 (0.74)	2.37 (0.29)	1.87 (0.22)		
$r_0$	0.924 (0.008)	0.918 (0.019)	0.929 (0.006)	0.927 (0.005)	0.924 (0.005)		
$r^2$	0.975	0.952	0.975	0.986	0.992		
$D_{Nd}$ -refit	0.015	0.313	0.012	0.015	0.008		
$D_{Sm}$ -refit	0.084	0.522	0.076	0.074	0.043		

Values in parentheses are uncertainties on  $D$  values propagated from standard deviations on SIMS intensities (10 cycles per point, three points per phase per experiment). AH83- KL2 is a SIMS standard basaltic glass; Meas. is composition measured treating standard as an unknown, Std. is the nominal composition.  $E$ ,  $D_0$ , and  $r_0$  are lattice-strain parameters from fits to Eq. (1) with calculated uncertainties in parentheses;  $r^2$  is multiple regression coefficient of determination for these fits. *Refits* are fit parameters calculated without including  $D_{Nd}$  and  $D_{Sm}$  as described in text.  $D_{Nd}$ -refit and  $D_{Sm}$  - refit are  $D$ s for Nd and Sm calculated from refit parameters.

incorporated along with some of the garnet analyses, thereby compromising the utility of measured  $D$  values, particularly those for highly incompatible elements such as the light REE. Melt could be incorporated either from overlap of the ion beam with large areas of melt adjacent to garnet crystals, or as submicron inclusions trapped within the grains themselves (any such inclusions would have to be smaller than what is resolvable using the electron microprobe's optics, as none were observed in back-scattered electron imaging). This possibility was examined in two ways. First, SIMS-analyzed run products were re-examined optically to verify the locations of pits formed by the beam, and any spots found to show visible overlap with adjacent melt were discarded (only two such points were found). Second, each SIMS analytical "cycle" was scrutinized to ensure that count rates were homogeneous throughout the analysis. As the analysis cycles proceed, the beam might have "drilled through" the garnet grain into melt lying beneath the plane of section of the mounted run product. We included Al and Mg in our list of analyte elements in order to monitor for this situation, because the large difference in content of these elements between garnet and coexisting melt would have been readily identifiable. We found that only a few individual sets of analytical cycles showed very minor evidence of such incorporation, and those likewise were omitted from further consideration.

Despite these precautions, we find that some melt incorporation did take place when analyzing some of the smallest garnet grains attempted (15–20  $\mu\text{m}$  in longest dimension). Fortunately, the systematics of lattice-strain modeling of partitioning allow us to correct for this problem. These issues will be detailed in Section 3 below.

### 3. Results

#### 3.1. Phase relations

Assemblages from experiments on A15C listed in Table 2 are plotted on a pressure–temperature diagram in Fig. 2. This plot also includes the  $P$ – $T$  points and mineral-in curves from the experiments of Elkins-Tanton et al. (2003). Our experiments require the existence of a point of multiple saturation with garnet and pyroxene at a pressure between 3.0 and 3.5 GPa (600–700 km lunar depth) and a temperature of  $\sim 1750$  °C. Our results require a slight inflection or curvature to the shape of the liquidus surface with increasing pressure, which is an occurrence observed in many high pressure studies when garnet becomes a near-liquidus phase. Overall, the position of the liquidus located by our experiments is quite compatible with that defined by the experiments of Elkins-Tanton et al. (2003). However, as described below, pyroxene in our experiments

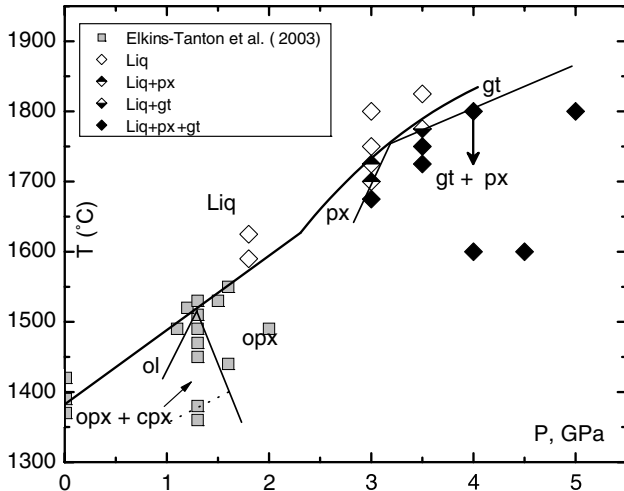


Fig. 2. Pressure–temperature diagram summarizing near-liquidus phase relations of A15C. Liq, quenched melt; ol, olivine; opx, orthopyroxene; cpx, clinopyroxene; px, supersolvus pyroxene; and gt, garnet. Low-pressure experiments (grey boxes) replotted from Elkins-Tanton et al. (2003). High-pressure point of multiple saturation is at 3–3.5 GPa,  $\sim 1750$  °C.

is a single, supersolvus phase in contrast to the two coexisting low- and high-Ca pyroxenes occurring in their experiments.

### 3.2. Phase compositions

Table 3 lists electron microprobe analyses of minerals and melts in all subliquidus experiments reported here. Garnet in our highest-pressure runs, A229 and A225, has a small but distinct majorite content, manifest by 3.06–3.12 Si and 1.70 to 1.61 Al, respectively, per 12-oxygen formula unit in the stoichiometry calculated from electron microprobe analyses. In this garnet, some Fe in octahedral coordination is required to fill the garnet octahedral (Y) site, as the only other trivalent cation available to enter Y is  $\text{Cr}^{3+}$ , and only 0.080–0.086 Cr per formula unit is available in those garnets. These changes reflect the enhanced solubility with increasing pressure of a pyroxene component,  $\text{R}_2^{2+}\text{Si}_2\text{O}_6$ , in the Y site of garnet,  $\text{R}_3^{2+}\text{R}_2^{3+}[\text{SiO}_4]_3$ , via the substitution  ${}^{\text{VI}}[\text{R}^{2+} + \text{Si}^{4+}] = 2{}^{\text{VI}}\text{R}^{3+}$  (Xirouchakis et al., 2002; Draper et al., 2003). In other words, majorite garnet is typified by some  $\text{Fe}^{2+}$  and  $\text{Si}^{4+}$  entering the Y site in octahedral coordination, causing Al per 12 oxygens to fall below 2.0 and Si per 12 oxygens to exceed 3.0, with some divalent cation(s) also entering Y for charge balance. Even small majorite contents probably play a role in affecting garnet-melt trace element D values, in similar fashion to data reported by Draper et al. (2003).

As mentioned above, pyroxenes formed in our experiments are single phase clinopyroxenes (pigeonite to low-Ca augite), compared to coexisting orthopyroxene + clinopyroxene at lower pressures as documented by Elkins-Tanton et al. (2003). Pyroxene compositions are more a function of temperature, and hence melt fraction,

at a given pressure than of pressure alone. These compositions at 3 GPa are  $\text{En}_{66}\text{Fs}_{18}\text{Wo}_{15}$  at 55% melt (run A8) and  $\text{En}_{56}\text{Fs}_{30}\text{Wo}_{14}$  at 22% melt (run A41); at 3.5 GPa,  $\text{En}_{65}\text{Fs}_{22}\text{Wo}_{13}$  at 65% melt (run A42); and at 5 GPa,  $\text{En}_{55}\text{Fs}_{24}\text{Wo}_{22}$  at 10% melt (melt fractions calculated by mass balance). Al contents of these pyroxenes range from 0.1 to 0.2 per 6-oxygen formula unit. Our pyroxenes compare favorably to those reported by Chen et al. (1982) from their experiments on Apollo 14 low-titanium green glass; relative to A15C this composition is 3 wt% poorer in  $\text{SiO}_2$  and has lower Mg# (56 vs. 67) and  $\text{CaO}/\text{Al}_2\text{O}_3$  (0.96 vs. 1.10). Their pyroxenes have ranges of  $\text{En}_{55-81}\text{Fs}_{14-27}\text{Wo}_{4-19}$  and 0.1–0.45 Al per formula unit at  $\sim 2$  GPa. We account for the presence of a single pyroxene in our experiments, instead of two pyroxenes as in those of Elkins-Tanton et al. (2003), by noting that our experimental temperatures are likely to be well above the high-pressure solvus in the pyroxene system. For comparison, experiments by Lindsley (1980) in the iron-free enstatite–diopside system show peak solvus temperatures at 3.0 GPa of  $\sim 1525$  °C, more than 100 °C cooler than the lowest-temperature run reported here, and the presence of Fe in the system would be expected to lower the solvus temperature even further. Lindsley (1980) also showed broad fields of a single clinopyroxene in iron-bearing systems at 3.0 GPa. Therefore, the appearance of only one pyroxene at our experimental conditions is not unexpected.

Electron microprobe totals for our quenched melts do not sum to 100% in most cases (Table 3). This deficiency results largely because ultramafic compositions like A15C are virtually impossible to quench to a glass at the high pressures of these experiments. Instead, quenched melts form extremely fine-grained (submicron to micron size), felty mats of ferromagnesian crystals that resemble komatiitic spinifex textures (Fig. 1). Textures like these have been reported from a wide variety of experimental studies of ultramafic compositions. For this reason we analyzed quenched melts with defocused beams, as indicated above. We assume that low totals reflect deficiencies in X-ray counts of all elements equally and are not due to a single element being incorrectly analyzed. This assumption is bolstered by repeated checks of microprobe standards and secondary standards (i.e., materials not used in calibration that were analyzed in multiple previous microprobe sessions), and by successful least-squares mass-balance mode calculations that yield quite good fits of the mineral and quenched melt compositions to that of the starting material (Table 2). For example, re-running these mass balance modes using melt compositions renormalized to 100% yields exactly identical modes.

### 3.3. Trace element partitioning values

Table 4 lists trace element partition coefficients from five doped experiments. Runs A221 and A225, although garnet-bearing, were too fine-grained to attempt SIMS analysis, with garnets ranging in size only to  $\sim 15$   $\mu\text{m}$ . Note

that the  $D$  values listed in Table 4 were calculated directly from the garnet/melt SIMS intensity ratios, as indicated above, in order to avoid propagation of any uncertainty arising from construction of calibration curves. Table 4 also includes a SIMS analysis of a standard basaltic glass that was treated as an unknown, compared to the nominal standard composition, as a measure of the accuracy of our SIMS data.

As mentioned above, some minor melt incorporation likely occurred in SIMS analyses of garnets, despite our best efforts to minimize it. For example,  $D$  values for the least garnet-compatible elements (Sr, Ba, Nd, and Th) in garnet from run A67 are significantly lower than they are in garnets from the other runs (Table 4). Those garnets are substantially smaller than are the garnets in run A67 (25–50  $\mu\text{m}$  in A138 and A140 compared to several hundred  $\mu\text{m}$  in A67). We infer that this contamination from melt incorporation was minor, except for run A138, because the  $D$  values for other elements such as Sc, Y, Zr, Hf, Dy, and Yb are quite similar between these experiments. Run A138 appears most strongly affected by melt incorporation, with the highest  $D$  values for Sr, Ba, and Th. As will be seen below,  $D$  values for the least compatible elements from the other four experiments can be well-constrained using fits to the lattice-strain partitioning model of Blundy and Wood (1994).

We compare the  $D$  values measured in our experiments with previously reported literature values in Figs. 3 (against experimental pressures) and 4 (against garnet composition). Fig. 3 illustrates significant differences between our  $D$  values and those from studies performed on magnesian compositions appropriate for terrestrial applications, in particular for Yb and Y.  $D$  values for Sm are slightly lower, whereas those for Nd, Hf, Sc, and Zr are similar. All these values are quite similar to  $D$  values measured in a chondritic composition by Draper et al. (2003) and to other, higher-pressure garnets in which garnets manifest a significant component of majorite. In contrast, in Fig. 4 our  $D$  values largely fall on trends of  $D$  vs. garnet composition established by previous studies of both magnesian, terrestrial compositions at low to high pressures and by our previous work on Fe-rich, chondritic compositions. These relationships are a consequence of garnet compositions in the experiments reported here being generally less pyropic at a given temperature and pressure than are garnets grown in more magnesian systems.

### 3.4. Lattice-strain partitioning model and correction for melt incorporation

#### 3.4.1. Lattice-strain model

The lattice-strain model of Blundy and Wood (1994) has been successfully applied to garnet-melt partitioning, in particular by van Westrenen and coworkers (van Westrenen et al., 1999, 2000, 2001a,b). The lattice-strain model fits partitioning data expressed in terms of  $D$  vs. ionic

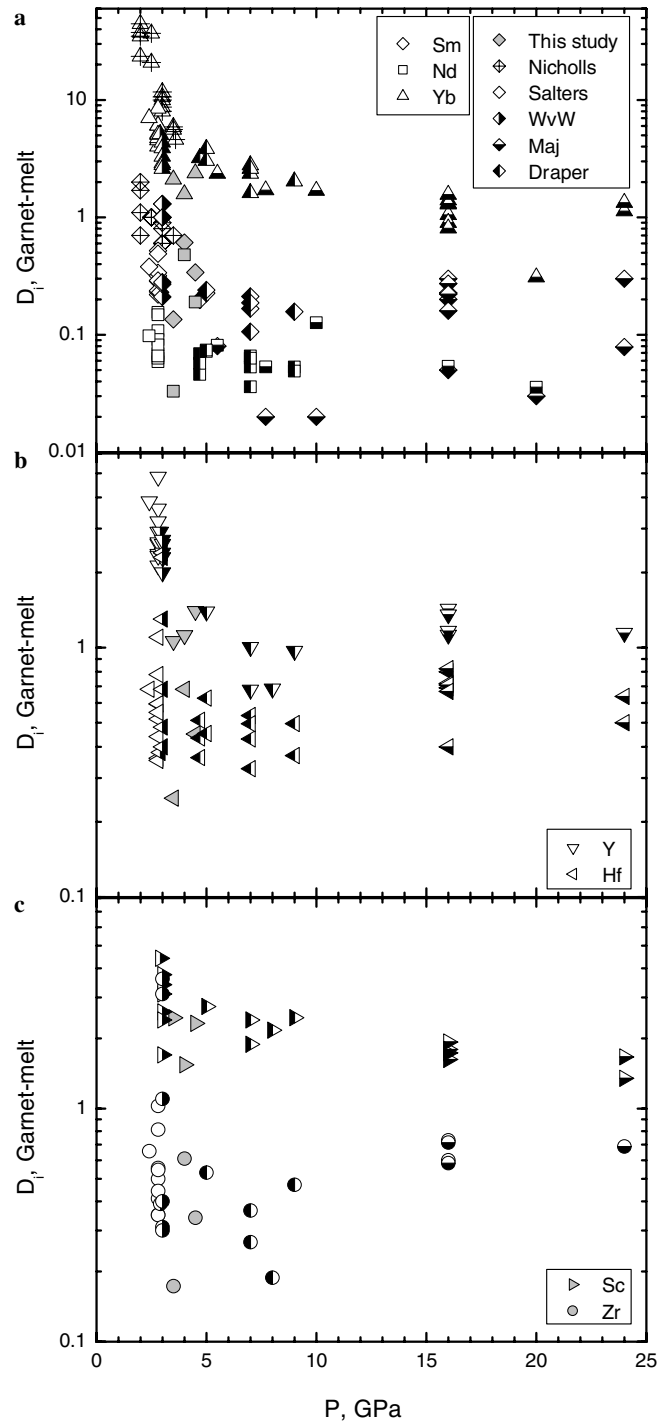


Fig. 3. Summary diagram comparing trace element  $D$  values as a function of pressure between this study and literature. (a), data on Sm, Nd, and Yb; (b), on Y and Hf; (c), on Sc and Zr. Symbol shapes keyed to various elements as given in legends (e.g., diamonds for Sm, inverted triangles for Y, circles for Zr), and symbol fills for different studies as denoted in legend; data from this study in light grey shading. Nicholls, Nicholls and Harris (1980); Salters, Salters et al. (2002); WvW, van Westrenen et al. (1999, 2000, 2001a); Maj, experiments producing majoritic garnet in Mg-rich systems (Kato et al., 1987; Ohtani et al., 1989; Yurimoto and Ohtani, 1992; Inoue et al., 2000; Suzuki et al., 2000); and Draper, mildly majoritic garnet in Fe-rich chondritic system (Draper et al., 2003). Note that most  $D$  values from A15C garnets are lower than virtually all previously published values, or fall at the low end of previously published ranges.

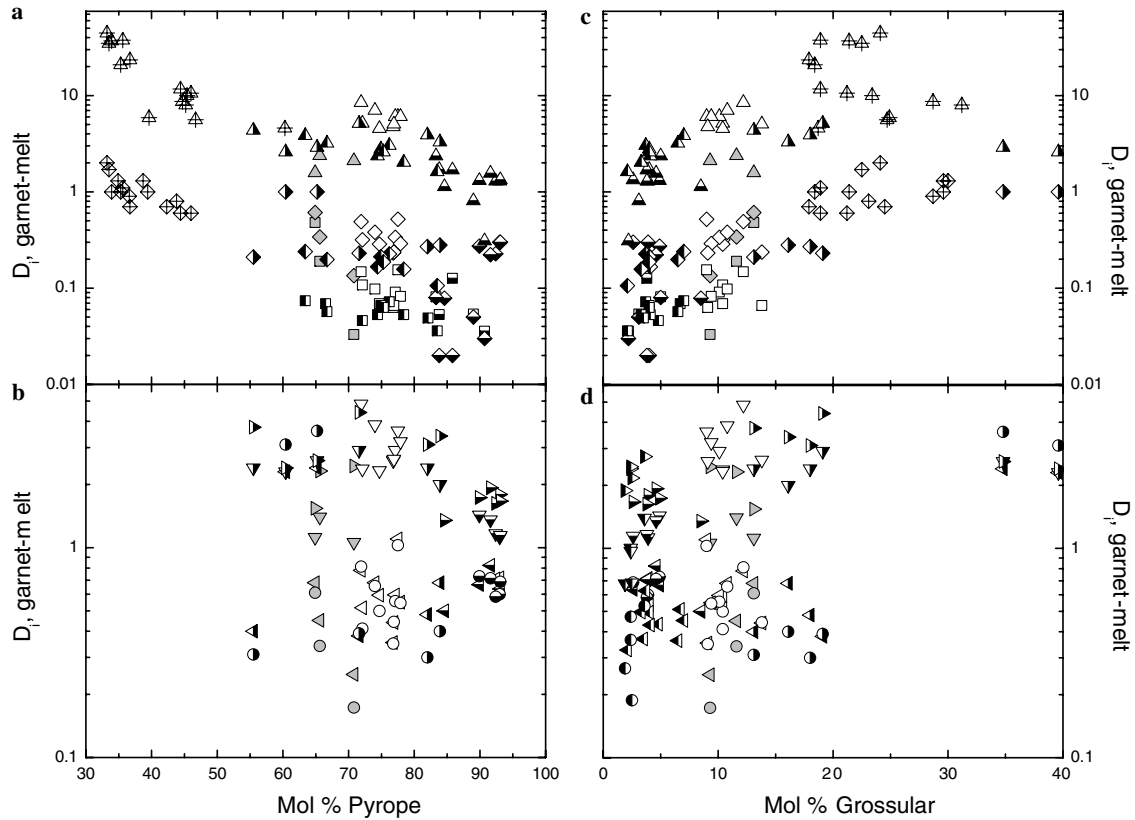


Fig. 4. Comparison of garnet-melt  $D$  values as a function of garnet composition between this study and literature values. (a, b)  $D$  vs. pyrope content; (c, d)  $D$  vs. grossular content. Data sources and symbols as in Fig. 3. Data from this study, although again falling at the lower end of ranges for previous data, generally fall on pre-existing trends of  $D$  values against garnet composition. See text for additional discussion.

radius; the pioneering work of Onuma et al. (1968) first described the parabolic trends of partitioning data on such plots. Blundy and coworkers drew on work by Brice (1975) to describe Onuma-type partitioning trends using

$$D_i = D_0 \times \exp \left[ \frac{-4\pi EN \left[ \frac{r_0}{2} (r_i - r_0)^2 + \frac{1}{3} (r_i - r_0)^3 \right]}{RT} \right], \quad (1)$$

where  $D_i$  is the measured partition coefficient for element  $i$ ,  $r_i$  is the ionic radius of that element,  $R$  is the gas constant,  $N$  is the Avogadro's number, and  $T$  is in Kelvins. This relationship is appropriate for describing partitioning of cations having the same charge into a given crystallographic site, for example trivalent cations partitioning into the garnet X site. Fits of partitioning data from a given experiment to Eq. (1) yield values for  $D_0$ , the maximum  $D$  value for a cation of that charge into that site;  $r_0$ , the ideal site size for strain-free partitioning of a cation of that charge; and  $E$ , the bulk (Young's) modulus, which can be considered a measure of site compressibility. Mathematically, these parameters correspond, respectively, to the  $y$ -intercept of maximum on the parabola; its  $x$ -intercept; and the width of the parabola (tighter curves yield higher  $E$ ). It is important for a meaningful fit that  $D$  values are available for elements having ionic radii both greater than and

less than the value of  $r_0$  so that both limbs of the parabola are constrained. For the trivalent cations partitioning into the garnet X site, this requirement is met when Sc is included in the collection of elements used in measuring partitioning, because its ionic radius (0.870 Å at coordination number 8; Shannon, 1976) is significantly below typical  $r_0$  values, while ionic radii for the rare earths are all greater. In general, if it can be shown that partitioning data for a set of isovalent cations follow this relationship, then Eq. (1) can be used to solve for the appropriate values of  $E$ ,  $D_0$ , and  $r_0$ , and these can in turn be used to calculate  $D_i$  for some unmeasured cation with radius  $i$ .

van Westrenen et al. (2001b) used data from several previous partitioning studies to form a predictive expression for trivalent cation partitioning in garnet. They related partitioning to temperature, pressure, garnet major-element composition, and garnet-melt  $D_{Mg}$ , to produce predicted values of  $D_0$ ,  $r_0$ , and  $E$  for use in Eq. (1) to calculate  $D$  values for systems in which partitioning has not been directly measured. This predictive relationship (termed "WvW predictive model" hereafter) was intended to cover pressures up to 7.5 GPa for largely basaltic compositional systems, and recovered published partitioning data not included in their parameterization quite successfully, to within ~20% relative. Applications of the WvW predictive model to garnet-melt partitioning in an Fe-rich, chondritic bulk compo-

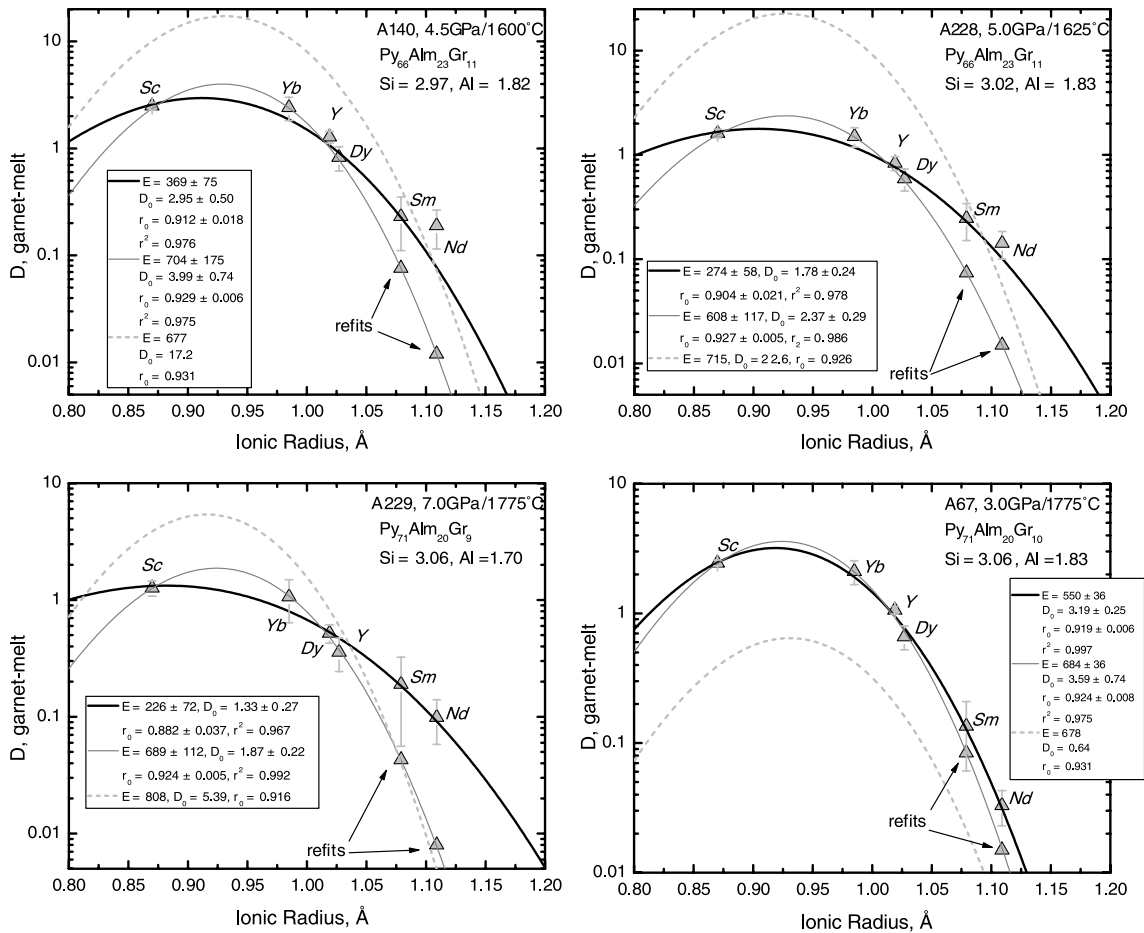


Fig. 5. Plot of trivalent  $D$  values (Table 4) against ionic radii from Shannon (1976) showing well-defined parabolic trends. Solid black curves are fit to lattice-strain model of Blundy and Wood (1994) Eq. (1), yielding parameters and uncertainties listed in legend. Solid grey curves are refits omitting  $D_{\text{Sm}}$  and  $D_{\text{Nd}}$  as described in text, with revised values for these, calculated from refit curves, shown labeled “Refits.” Dashed curves are partitioning predicted by formulation of van Westrenen et al. (2001b). Note large mismatches between observed and predicted partitioning, especially in  $D_0$ .

sition in which garnets had an appreciable majorite component yielded substantial mismatches between the predicted and measured partitioning behavior (Draper et al., 2003). Accordingly, we sought to determine whether their relationship could successfully predict partitioning in our runs on A15C, and in fact one aim of the experiments reported here is to provide additional data coverage on garnet-melt partitioning in order to expand the applicability of the WvW predictive model beyond terrestrial compositions at comparatively low pressures. This effort has already yielded revised predictive expressions that account for partitioning in anhydrous, Fe-rich systems much better than previously (Draper and van Westrenen, 2005).

Our trivalent partitioning data (Nd, Sm, Dy, Y, Yb, and Sc, Table 4) yield good fits to Eq. (1), and once again our measured values are not reproduced by the WvW predictive model. Fig. 5 summarizes these results for runs A67, A140, A228, and A229. (We do not consider further data from A138, which we judge experienced far more substantial melt incorporation than the other runs listed in Table 4.) On all plots, solid curves are fits to Eq. (1) of our measured  $D$  values from each experiment, and dashed curves represent the partitioning predicted by the WvW model.

It is clear that the WvW model predicts substantially larger  $D$  values than those measured for virtually all trivalent cations. Table 4 also lists the values of the fit parameters  $E$ ,  $r_0$ , and  $D_0$  resulting from application of Eq. (1) to the data from each experiment.

A major difference between  $D$  values in our garnets and those from previous studies is that the parabolic curves formed by our data on plots like those in Fig. 5 are broader than those from the earlier work. Broader parabolae correspond to lower values of  $E$ , indicating greater compressibility of the X site in these garnets. Detailed crystal-chemical treatment of factors affecting how the lattice-strain fit parameters change with pressure, temperature, and composition are the subject of separate contributions (e.g., Draper and van Westrenen, 2005), but briefly put, these low apparent  $E$  values are probably anomalously so, even taking into account the expectation from our previous work (Draper et al., 2003) that  $E$  is typically lower in more Fe-rich garnets. As described above, we suspect some melt incorporation took place in many of the SIMS analyses, and the effect of such incorporation would be to artificially elevate the  $D$  values somewhat for the least-compatible elements. This would in turn lead to broader parabolae, and

hence lower values of  $E$ . The lattice-strain model, fortunately, provides a powerful tool for quantifying the extent of that incorporation and for correcting for it.

### 3.4.2. Correcting for melt incorporation in garnet SIMS analyses

To assess the possible effects of melt incorporation in the SIMS analyses of experimental garnets, we refit our  $D$  values from each of the four experiments cited above to Eq. (1), but omitted  $D_{\text{Sm}}$  and  $D_{\text{Nd}}$  from the fits. In other words, the refit parabolae were constrained by  $D$  values for Sc, Y, Yb, and Dy. Because these four elements span a sufficient range of ionic radius, and in particular provide points on both limbs of the curves (i.e., at ionic radii both higher and lower than the likely range of  $D_0$  values), a mathematically robust fit still results. The refit curves are documented in the lower portion of Table 4, where the new fit parameters are listed along with their calculated uncertainties. Fig. 5 also includes curves (light grey) generated from these refits. Note that the refit curves account for the  $D$  values for Sc, Yb, Y, and Dy at least as well as, if not better than, the original fits, as judged by the  $r^2$  values that are in most cases higher than those from the original fits. Table 4 also includes values of  $D_{\text{Sm}}$  and  $D_{\text{Nd}}$  calculated using Eq. (1) from the refit parameters as outlined in the preceding section. For runs A140, A228, and A229 the revised values are significantly lower than the original measurements, whereas the difference for A67 is much less (recall that A67 had substantially larger garnets than did the other experiments). The revised  $D_{\text{Sm}}$  and  $D_{\text{Nd}}$  values are also plotted in Fig. 5. Finally, note that the effect of minor melt incorporation on the four elements used in the refits is expected to be very small, given that those elements are either compatible in garnet or only slightly incompatible. In other words, it takes only a very small amount of melt incorporation to compromise  $D$  values for highly incompatible elements, but that same amount of incorporation has a comparatively trivial effect on more-compatible elements because melt contains comparatively less of the compatible elements, by definition.

Another check on the quality of our partitioning data is shown in Fig. 6. Here, we plot  $D_{\text{Yb}}$  vs.  $D_{\text{Sm}}$  for garnets from this work and many previously published studies (Nicholls and Harris, 1980; Kato et al., 1988; Ohtani et al., 1989; Salters and Longhi, 1999; van Westrenen et al., 1999, 2001a; Barth et al., 2002; Salters et al., 2002; Draper et al., 2003; Corgne and Wood, 2004; Pertermann et al., 2004). Overall, a linear relationship is expected on this log-log diagram, and this is broadly true of many, but not all, of the data shown in Fig. 6.  $D$  values for these elements as measured in the four experiments mentioned above are connected to their revised values with horizontal arrows; that is,  $D_{\text{Yb}}$  remains essentially unchanged while  $D_{\text{Sm}}$  decreases as a result of the refit procedure outlined above. Although the as-measured values were not greatly displaced from the main trend, their revised positions are significantly closer to

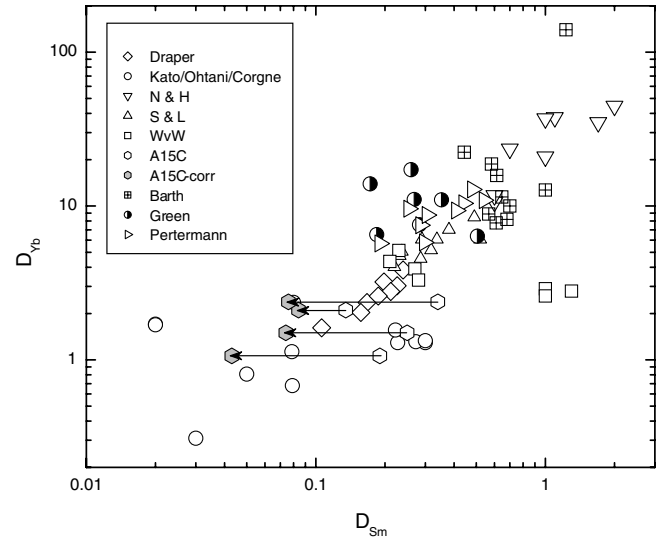


Fig. 6. Plot of  $D_{\text{Yb}}$  vs.  $D_{\text{Sm}}$  comparing measured and corrected  $D_{\text{Sm}}$ . Data sources: Draper, majoritic garnets in Fe-rich chondrite melt, Draper et al. (2003); Kato/Ohtani/Corgne, majoritic garnets in more magnesian melt, Kato et al. (1988), Ohtani et al. (1989), Corgne and Wood (2004); N and H, garnets in basaltic to andesitic melt, Nicholls and Harris (1980); S and L, garnets in basaltic melt, Salters and Longhi (1999) and Salters et al. (2002); Barth and Green, garnet in hydrous basaltic melt, Barth et al. (2002) and Green and Blundy (unpublished); Pertermann, garnet in eclogitic melt, Pertermann et al. (2004). Original  $D_{\text{Sm}}$  measurements from this study are connected to their revised values by horizontal arrows. Note that revised values fall closer to overall trend than do measured values.

it. This situation lends additional confidence that the revisions to our  $D_{\text{Sm}}$  and  $D_{\text{Nd}}$  values are reasonable. The downward revisions of these two values may seem large at first glance, being a factor of two to ten smaller; however, as we show below, these changes do not affect the conclusions drawn from use of these data in petrogenetic models of low-Ti lunar liquid genesis.

How much melt was incorporated in these “suspect” garnet analyses? We can assess this question in a qualitative sense using the batch-melting equation,  $C_L/C_0 = 1/(F + D - FD)$ , where  $C_L$  is the element concentration in the liquid,  $C_0$  is the starting composition for that element,  $F$  is the melt fraction of an experiment, and  $D$  is the bulk partition coefficient. If we assume that  $C_0$  for Sm and Nd = 25.3 and 17.6 ppm, respectively (Table 1), we can calculate how  $C_L/C_0$  would differ when using the as-measured  $D$  values, as opposed to the corrected values. Using run A229 as an example (because it consists of only garnet and liquid; we did not measure  $D$  values in pyroxene so cannot calculate a bulk  $D$  for runs containing both pyroxene and garnet), with  $F = 0.89$  (by mass balance, Table 2), we find that for Sm,  $C_L/C_0 = 1.098$  if the as-measured  $D_{\text{Sm}}$  is used, and 1.118 if the corrected value is used. For Nd, the corresponding  $C_L/C_0 = 1.110$  for as-measured  $D_{\text{Nd}}$  and 1.122 for the corrected  $D_{\text{Nd}}$ . These differences correspond to the quenched melt in this experiment having 27.8 ppm Sm and 19.5 ppm Nd using the as-measured  $D$  values compared to

28.3 ppm Sm and 19.7 ppm Nd for the corrected  $D$  values. These slight changes, well below the analytical uncertainties for these elements cited in Table 1, suggest that the amount of melt incorporation in garnet SIMS analyses was in fact very small.

Fits of our tetravalent data to Eq. (1) are unfortunately not feasible, because the range of ionic radii of the  $4^+$  cations present in our experiments (Ti, Hf, Zr, and Th) is not sufficiently large to yield a robust fit. The expected ideal site size  $r_0$  for the garnet Y site is on the order of 0.7 Å, and the ionic radii of our  $4^+$  cations are all approximately equal to or larger than this value. As a result, all data would fall on one limb of the parabola, up to its peak, but without a datum on the opposite limb, so no meaningful fit to Eq. (1) is possible. There is a potential solution to this dilemma for garnets having a significant majorite component. In such a case, a  $D$  value for Si in octahedral coordination ( $^{VI}\text{Si}$ ) could be calculated, and because the ionic radius of 6-coordinated  $\text{Si}^{4+}$  is 0.40 Å (Shannon, 1976), a fit to Eq. (1) would be mathematically obtainable. However, it is not clear whether a putative  $D$  for  $^{VI}\text{Si}$  would use in its denominator the total amount of Si in the melt or only some fraction that could be shown to be in octahedral coordination in the liquid phase. Such considerations are well beyond the scope of this contribution, and future work will take doped A15C to higher pressures in an effort to apply the lattice-strain model to tetravalent element partitioning by growing garnets having a significant majorite component while evaluating the role of Si coordination in coexisting melt.

In any case, we are now in a position to supply partitioning values for low-Ti lunar compositions for any trivalent cation entering the garnet X site by using the  $D$  values measured and revised from use of Eq. (1). We can use directly the values we actually measured in our experiments, and can derive any unmeasured trivalent  $D$  value by using the values of  $r_0$ ,  $D_0$ , and  $E$  that result from fits of our partitioning data to Eq. (1) and calculating  $D$  given that unmeasured element's ionic radius. This study therefore provides the first garnet-melt partitioning data from compositions directly relevant to the lunar interior, in contrast to having to rely on  $D$  values taken from experiments on very different, “terrestrial” bulk compositions. In the following sections, we apply these new  $D$  values to previously published work in which the role of garnet was assessed in part by making use of garnet partitioning values taken from these earlier “terrestrial” studies.

#### 4. Discussion: Garnet in low-Ti picrite glass source?

##### 4.1. Model of Beard et al. (1998)

Beard et al. (1998) (“B98” hereafter) measured Lu–Hf isotopic systematics for a range of mare basalts and showed that low-Ti and high-Ti lunar magmas likely originated from distinct source regions, with the source for low-Ti basalts having chondrite-normalized Lu/Hf approximately

four times that for high-Ti basalts. They argued that these results could best be explained by polybaric melting of an initially garnet-bearing source, with garnet being consumed as the melting regime moves to shallower levels and into the spinel stability field. Such a model generated liquids having the required Lu/Hf fractionations while having last equilibrated with a residuum consisting dominantly of olivine and orthopyroxene. However, that model was calculated using garnet  $D$  values from the available literature at the time, and as indicated above the experimental partitioning data for garnet all came from studies performed on terrestrial compositions that are quite different from lunar ones (see Beard et al., 1998, for references). Specifically, the garnet  $D$  values they used for Sm, Nd, Lu, and Hf were 0.25, 0.15, 8.05, and 0.27, respectively, yielding  $D_{\text{Sm}}/D_{\text{Nd}} = 1.67$  and  $D_{\text{Lu}}/D_{\text{Hf}} = 29.8$ .

Here, we recalculate the B98 non-modal batch melting model, which employed data on Sm, Nd, Lu, and Hf, using  $D$  values obtained from this study. First, we simply recalculated the B98 model 2A, which those authors suggested best accounted for their low-Ti mare basalt results and was set up with 2% garnet in the source. In each set of calculations, we used both the as-measured  $D$  values from runs A67, A140, A228, and A229 and the corrected values for  $D_{\text{Sm}}$  and  $D_{\text{Nd}}$  as outlined in the preceding section and listed in Table 4. Also,  $D_{\text{Lu}}$  was calculated from fit parameters to Eq. (1), both with and without as-measured  $D_{\text{Sm}}$  and  $D_{\text{Nd}}$  to generate the fits. For runs A67, A140, A228, and A229, respectively, these  $D_{\text{Lu}}$  values are 2.14–2.38; 2.05–2.73; 1.27–1.67; and 0.86–1.24. We therefore have, for each of the four experiments used, a pair of  $D$  values for each of the four elements of interest. The corresponding  $D$  ratios for these four runs range from 1.2 to 6.3 (average 3.93) for  $D_{\text{Sm}}/D_{\text{Nd}}$  and 3.3 to 9.6 (average 6.52) for  $D_{\text{Lu}}/D_{\text{Hf}}$ . It is immediately evident from these values, compared to those used in the original B98 model, that calculated melting paths should differ substantially using our new partitioning data.

Recalculated model results are plotted in Fig. 7, which consists of modified versions of Fig. 10 of Beard et al. (1998) and focuses on the model they designated “2A,” the garnet-bearing model (2% garnet in source) that appears to best fit their measured data. The parameters  $\delta[\text{Lu}/\text{Hf}]_n$  and  $\delta[\text{Sm}/\text{Nd}]_n$  in Fig. 7 are ways of normalizing measured ratios in a lava or melt to values for the lava's source region calculated from isotope data, similar to the definition of Salters and Hart (1989).  $\delta[\text{Lu}/\text{Hf}]_n$  is defined as  $([\text{Lu}/\text{Hf}]_n^{\text{source}} - [\text{Lu}/\text{Hf}]_n^{\text{lava}})/[\text{Lu}/\text{Hf}]_n^{\text{source}}$ , and  $\delta[\text{Sm}/\text{Nd}]_n$  is defined in analogous fashion; see Beard et al. (1998) for full details. In Fig. 7A, their original model 2A curve is plotted in open grey circles (“Original model” in legend), up to 1% melting, by which point the garnet initially present is held to have been consumed. This curve reaches the high  $\delta[\text{Lu}/\text{Hf}]_n$  end of the set of low-Ti mare basalt compositions plotted (grey diamonds), and subsequent melting to higher melt fractions yields trends that closely mimic those data; that part of the melting curve is omitted for clarity. For comparison, the same model curve is recalculated changing nothing but the

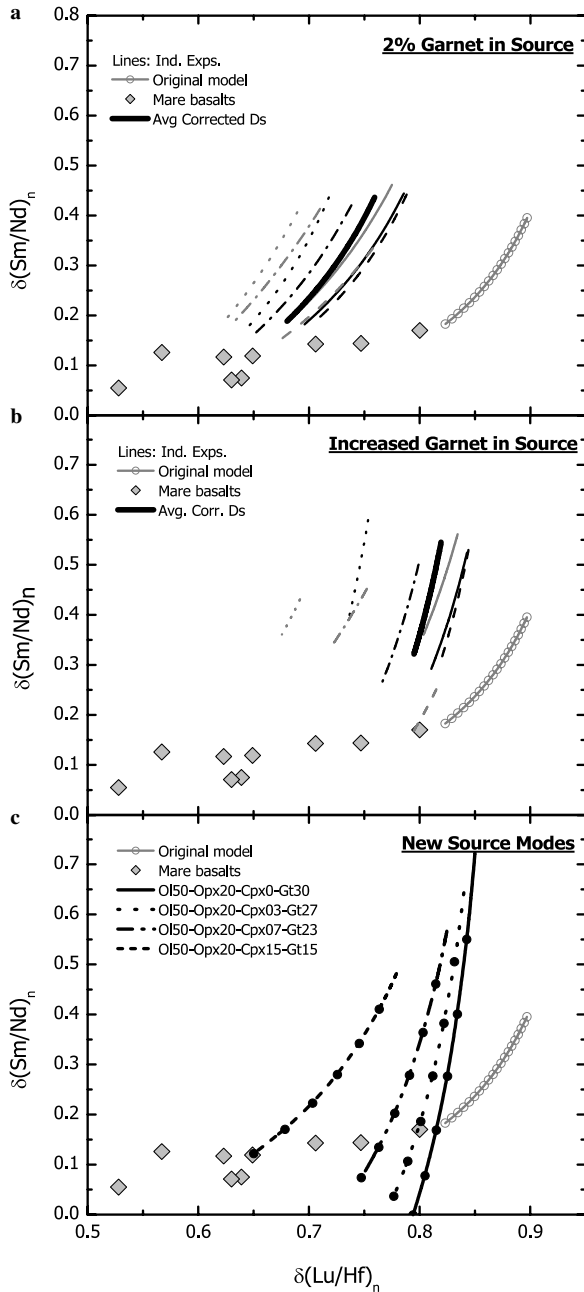


Fig. 7. Results of batch melting calculations similar to those summarized in Fig. 10 of Beard et al. (1998). Grey diamonds are low-Ti lunar basalts. (a) Identical model to Beard et al. (1998) with 2% garnet in source, but using the  $D$  values for Sm, Nd, Lu, and Hf from this study rather than those available previously from experiments on terrestrial compositions. Original model is Model 2A curve calculated by Beard et al. (1998). Our curves calculated using data from individual experiments (“Ind. Exps.”) A67, A140, A228, and A229 shown with both measured and revised values of  $D_{Sm}$  and  $D_{Nd}$ ; heavy curve is result when using average of revised  $D$  values. All curves depict 0–1% partial melting. (b) Model with source garnet content increased in proportion to lower  $D_{Lu}/D_{Hf}$  ratio from our  $D$  values compared to previous values. Curves are shown using corrected  $D$  values used for individual experiments and heavy curve uses average of revised values; all curves depict 0–1% melting as in (a). (c) Models using different source modes in attempt to reach similar compositions as 1% melt in original Beard et al. (1998) Model 2A. Dots signify 1% melt increments. Only garnet-rich, clinopyroxene-poor or -absent sources reach the target values. See text for discussion.

$D$  values for Sm, Nd, Lu, and Hf as indicated above. These results are shown in families of curves, one pair from the data for each individual experiment from both the as-measured and corrected  $D$  values (“Ind. Exps.” in legend); those curves also terminate at 1% melting. Note that the positions of curves calculated from each individual experiment shift only to a small extent by using the corrected  $D$  values. This observation lends support to our inference that the magnitude of melt incorporation in our garnet SIMS analyses is minor; no change to model conclusions would ensue from use of one or the other set of data. For the remainder of the discussion, then, we will focus on models calculated using the corrected values, given that they yield more realistic inferences about garnet crystal chemistry as mentioned above. Accordingly, we also plot model results in Fig. 7A calculated using the average of the corrected  $D$  values, shown as the heavy curve. All of the new curves intersect the set of low-Ti data at far lower values of  $\delta[Lu/Hf]_n$  than in the original model, and subsequent melting produces trends that intersect the field of low-Ti data points only at the lowest values of  $\delta[Lu/Hf]_n$  (also not shown for clarity). From these results, we conclude that the source lithology used in the original B98 model, with 2% garnet, cannot produce liquids having the Sm/Nd and Lu/Hf signatures measured by Beard et al. (1998) because the garnet that can actually be in equilibrium with A15C melt does not partition Sm, Nd, Lu, and Hf correctly.

Could the modeling be reconciled with our new  $D$  values if the amount of garnet in the source being melted is increased? One might suppose that increasing source garnet content in proportion to the change in  $D_{Lu}/D_{Hf}$ , which is a factor of 3.1–9.0 (average 4.6) lower using our new  $D$  values than the value used by Beard et al. (1998) in their models, might succeed in doing so. Fig. 7B examines this possibility, again comparing the original B98 model in grey circles with melting trends calculated by scaling up the garnet content of the source in proportion to those differing ratios (i.e., garnet contents of 6–18%, average 9.2%), reducing the modes of olivine and pyroxene in proportion to their mode in the original model. Here, we plot curves only for the corrected  $D$  values from each of the four experiments we have been using, again terminating at 1% melting, along with a heavy curve calculated using average corrected  $D$  values. Clearly, these trends also do not come close to the 1% melt endpoint of the original model 2A, and in order to intersect the trend of low-Ti data points, melting must proceed to 2–3%, higher than the value at which it was assumed that garnet would be consumed. Also, increased degrees of melting yield curves that range to values of  $\delta[Sm/Nd]_n$  much too low to match the low-Ti mare trend. In addition, contents of garnet in the deep lunar mantle as high as 6–18% do not seem realistic.

Finally, in Fig. 7C we calculate melting curves for a variety of arbitrarily chosen source lithologies to try to reproduce the 1% melt endpoint of the original model 2A curve. In these four curves, we assume a source

consisting of 50% olivine and 20% orthopyroxene, with the remainder some combination of clinopyroxene and garnet (assuming that only those two phases have the capacity to impart fractionations in Sm, Nd, Lu, and Hf); the four modes chosen are given in the legend. The closest matches to the target value come from sources having ~30% garnet that are either devoid of clinopyroxene or have only a few percent of that mineral, melting to ~6%. Clearly such lithologies are inconsistent with the olivine- and orthopyroxene-dominated assemblages thought to typify the lunar mantle.

#### 4.2. Ramifications for possible role of garnet

There are essentially three possibilities regarding the role of garnet in the formation of lunar liquids. Either garnet was present in the source initially, and remained in the residue after melting; or it was present initially but was consumed during low-degree melting; or it was never present in the source rocks at all. We can use our experimental results to assess these three possibilities for very low-Ti lunar liquids in the following ways.

If garnet was in the source for A15C and was not consumed upon melting, then we would expect to find, at the pressure–temperature conditions at which the liquid was separated from its residue, that (a) garnet was on the liquidus and (b) that it partitioned trace elements in such a way as to yield reasonable matches to the trace-element compositions of low-Ti lunar liquids. For the experiments reported here, the first of these conditions is met: there is a broad  $P$ – $T$  range of near-liquidus garnet stability. However, as outlined above, the second condition is not met: these garnets do not have trace element  $D$  values that can produce such a match for the trace element compositions of very low-Ti lunar basalts or picrite glasses.

The expected experimental observations if garnet was initially present in the A15C source but was consumed upon melting are slightly more complicated. In such a case, we would neither expect nor require that trace-element contents of low-Ti lunar liquids match the patterns that would arise from partitioning imposed by garnet, because at melt separation, there would be no garnet surviving to impose such signatures. Furthermore, at the conditions of melt extraction, we would expect NOT to find garnet as a liquidus phase, because by that stage, garnet would have been consumed and therefore not present to saturate the liquid at that point in its petrogenesis. This is a fundamental requirement of the near-liquidus, inverse-approach experiments performed in this study. Again, the first of these conditions is met: there is no match between the trace element patterns in low-Ti lunar liquids and those that would be imposed by garnet that partitions trace elements as measured here. However, the second condition is not met: we do in fact observe liquidus garnet, and over a substantial range of  $P$ – $T$  conditions. It is likely, although we cannot prove it solely from the work documented here, that this

range of  $P$ – $T$  conditions encompasses that at which garnet could have been present in lunar source lithologies. Furthermore, we cannot rule out the possibility that garnet was present in the source rocks at pressures between ~2.0 and 2.5 GPa, where we have no experimental coverage (Fig. 2), although we note that rather restricted conditions would be required in order for this to be possible.

Finally, if garnet took no role in the formation of low-Ti lunar liquids, either by having once been present in the source or by persisting in the residue after melting, then finding near-liquidus garnet would be essentially irrelevant, and a result of simply taking a liquid of basaltic (*sensu lato*) composition to high enough pressure to form garnet (which virtually every basalt will eventually do if the pressure is sufficiently high). Given that A15C displays a lower-pressure multiple saturation point (Elkins-Tanton et al., 2003) with a quite reasonable lunar mantle mineral assemblage, we can infer (although we cannot prove) that our experiments are consistent with garnet having played no role whatever in the formation of A15C melt.

We therefore make the following conclusions from interpretation of our high-pressure experimental results on phase relations and element partitioning. Although garnet is the liquidus phase for A15C at high pressure, the point of multiple saturation defined by our experiments requires a residual lithology that is unlikely to be appropriate for lunar mantle, e.g., Hess (2000). Were olivine to occur along with garnet and pyroxene near the liquidus of A15C, a much more convincing case for a garnet-bearing source could be made. In addition, the ~3 GPa liquidus temperature of ~1750 °C, although not incompatible with most lunar thermal models, is at the high end of the range of likely temperatures for depths of 600–700 km at the time of peak lunar magmatism, e.g., models summarized in Basaltic Volcanism Study Project (1981). Accordingly, we conclude that the multiple saturation point identified by Elkins-Tanton et al. (2003) remains the more appropriate, representing at least the minimum depth of melting for this composition. In principle, our multiple saturation point could then represent a maximum depth of melting. In addition, the occurrence of single-phase pyroxenes, although straightforward to understand thermochemically, is not in agreement with the clinopyroxene + orthopyroxene expected in the lunar mantle. We therefore do not believe the high-pressure point of multiple saturation found for liquid A15C with garnet and pyroxene at ~3 GPa represents the conditions at which, or source lithology in which, melting occurred to produce the most titanium-poor lunar glasses.

Taken together, considerations of both the phase relations and element partitioning in the Apollo 15 green C composition lead us to conclude also that garnet was not in the residue of melting that produced the A15C lunar picrite glass, nor, by extension, in residua for other very low-Ti lunar liquids. Even though A15C is saturated with garnet at high pressure, the garnet that is in equilibrium with such liquids simply does not partition Sm, Nd, Lu, and Hf in such a way as to explain low-Ti lunar

compositions. In addition, REE patterns for Apollo 15 low-Ti picrite glasses are generally flat to slightly LREE depleted (Steele et al., 1992; Shearer and Papike, 1993; Shearer et al., 2003), without the light REE enrichments that would be produced by residual garnet of any type, both “terrestrial” (using D values from previous literature) and lunar (D values from this study). By elimination, then, and applying the inferences outlined above, our experimental results are consistent with garnet never having been present in the source rocks of this lunar liquid. This conclusion is, however, at odds with the observation by Beard et al. (1998) that a Lu-retentive phase played a role in the formation of the source regions for low-Ti lunar compositions. We could speculate that the features identified in the isotopic measurements of Beard et al. (1998) were imparted on the low-Ti source regions through early magma ocean crystallization processes or result from an initial lunar composition that is not chondritic with respect to Lu and Hf; evaluating such possibilities is beyond the scope of this contribution.

## 5. Summary and conclusions

The Apollo 15 green C picritic glass is saturated with garnet and single-phase pyroxene between 3.0 and 3.5 GPa (600–700 km lunar depth) and a temperature of ~1750 °C. This olivine-free assemblage is not likely to represent the lithology of the lunar mantle. However, the coexistence of garnet with A15C liquid allows us to measure partitioning values for important trace elements, and thus assess the geochemical signatures that should arise if A15C were in fact derived from a garnet-bearing source. The results of these calculations do not support the notion that garnet was present in the residues of melting that produced very low-Ti lunar liquids like A15C. We infer, furthermore, that garnet probably was not involved at any stage of the formation of these melts.

## Acknowledgments

We are very grateful to Dr. Linda Elkins-Tanton for generously providing us with the A15C powder from her earlier study. D.S.D. thanks Dr. A. Dana Johnston for his hospitality while visiting the University of Oregon experimental petrology laboratory and Dr. Lars Borg for helpful lunar and isotopic discussions. We thank Mr. Paul Burger for constructing the trace element solution used in these and other experiments. Drs. Linda Elkins-Tanton, John Jones, and John Longhi provided very useful journal reviews. This research was supported by National Science Foundation Grant EAR-0337237 to D.S.D. and by National Aeronautics and Space Administration Cosmochemistry Grant 133388 to C.B. Agee.

## References

- Agee, C.B., Li, J., Shannon, M.C., Circone, S., 1995. Pressure–temperature phase diagram for the Allende Meteorite. *J. Geophys. Res.* **100**, 17,725–17,740.
- Barth, M.G., Foley, S.F., Horn, I., 2002. Partial melting in Archean subduction zones: constraints from experimentally determined trace element partition coefficients between eclogitic minerals and tonalite melts under upper mantle conditions. *Precamb. Res.* **113**, 323–340.
- Basaltic Volcanism Study Project, 1981. *Basaltic Volcanism on the Terrestrial Planets*. Pergamon Press.
- Beard, B.L., Taylor, L.A., Scherer, E.E., Johnson, C.M., Snyder, G.A., 1998. The source region and melting mineralogy of high-titanium and low-titanium lunar basalts deduced from Lu–Hf isotope data. *Geochim. Cosmochim. Acta* **62**, 525–544.
- Blundy, J., Wood, B., 1994. Prediction of crystal–melt partition coefficients from elastic moduli. *Nature* **372**, 452–454.
- Brice, J.C., 1975. Some thermodynamic aspects of the growth of strained crystals. *J. Cryst. Growth* **28**, 249–253.
- Chen, H.K., Delano, J.W., Lindsley, D.H., 1982. Chemistry and phase relations of VLT volcanic glasses from Apollo 14 and Apollo 17. *Lunar Planet. Sci. Conf. 13th, Proc.* **87**, A171–A181.
- Chen, H.K., Lindsley, D.H., 1983. Apollo 14 very low titanium glasses: melting experiments in iron–platinum alloy capsules. *Lunar Planet. Sci. Conf. 14th, Proc.* **88**, 335–342.
- Corgne, A., Wood, B., 2004. Trace element partitioning between majoritic garnet and silicate melt at 25 GPa. *Phys. Earth Planet. Int.* **143–144**, 407–419.
- Delano, J.W., 1980. Chemistry and liquidus phase relations of Apollo 15 red glass: implications for the deep lunar interior. *Lunar Planet. Sci. Conf. 11th, Proc.*, 251–288.
- Delano, J.W., 1986. Pristine lunar glasses; criteria, data, and implications. *Lunar Planet. Sci. Conf. 16th, Proc.* **91**, D201–D213.
- Draper, D.S., du Frane, S.A., Shearer, C.K., 2004. Preliminary high pressure phase relations of Apollo 15 green C glass: assessment of the role of garnet. *Lunar Planet. Sci.* **XXXV**, 1297.
- Draper, D.S., van Westrenen, W., 2005. An updated predictive model for garnet–melt trace element partitioning. *Eos, Trans. Am. Geophys. Union* **86**, V41E–1504.
- Draper, D.S., Xirouchakis, D., Agee, C.B., 2003. Trace element partitioning between garnet and chondritic melt from 5 to 9 GPa: implications for the onset of the majoritic transition in the Martian mantle. *Phys. Earth Planet. Interiors* **139**, 149–169.
- Elkins, L.T., Fernandes, V.A., Delano, J.W., Grove, T.L., 2000. Origin of lunar ultramafic green glasses; constraints from phase equilibrium studies. *Geochim. Cosmochim. Acta* **64**, 2339–2350.
- Elkins-Tanton, L.T., Chatterjee, N., Grove, T.L., 2003. Experimental and petrological constraints on lunar differentiation from the Apollo 15 green picritic glasses. *Meteorit. Planet. Sci.* **38**, 515–527.
- Green, D.H., Ringwood, A.E., Hibberson, W.O., Ware, N.G., 1975. Experimental petrology of Apollo 17 mare basalts. *Lunar Sci. Conf. 6th, Proc.* **6**, 871–893.
- Green, D.H., Ringwood, A.E., Ware, N.G., Hibberson, W.O., Major, A., Kiss, E., 1971a. Experimental petrology and petrogenesis of Apollo 12 basalts. *Lunar Sci. Conf. 2nd, Proc.* **2**, 601–615.
- Green, D.H., Ware, N.G., Hibberson, W.O., Major, A., 1971b. Experimental petrology of Apollo 12 basalts; part 1, Sample 12009. *Earth Planet. Sci. Lett.* **13**, 85–96.
- Grove, T.L., Vaniman, D.T., 1978. Experimental petrology of very low Ti (VLT) basalts. In: Merrill, R.B., Papike, J.J. (Eds.), *Conference on Luna 24: Mare Crisium*. Pergamon, pp. 445–471.
- Hess, P.C., 2000. On the source regions for mare picrite glasses. *New views of the Moon: Part 1* **105**, 4347–4360.
- Hess, P.C., Parmentier, E.M., 1995. A model for the thermal and chemical evolution of the Moon’s interior: implications for the onset of mare volcanism. *Earth Planet. Sci. Lett.* **134**, 501–514.

- Hodges, F.N., Kushiro, I., 1974. Apollo 17 petrology and experimental determination of differentiation sequences in model Moon compositions. *Lunar Sci. Conf. 5th, Proc.*, 505–520.
- Inoue, T., Rapp, R.P., Zhang, J., Gasparik, T., Weidner, D.J., Irifune, T., 2000. Garnet fractionation in a hydrous magma ocean and the origin of Al-depleted komatiites: melting experiments of hydrous pyrolyte with REEs at high pressure. *Earth Planet. Sci. Lett.* **177**, 81–87.
- Kato, T., Irifune, T., Ringwood, A.E., 1987. Majorite partition behavior and petrogenesis of the Earth's upper mantle. *Geophys. Res. Lett.* **14**, 546–549.
- Kato, T., Ringwood, A.E., Irifune, T., 1988. Experimental determination of element partitioning between silicate perovskites, garnets and liquids: constraints on early differentiation of the mantle. *Earth Planet. Sci. Lett.* **89**, 123–145.
- Kesson, S.E., 1975. Mare basalts: melting experiments and petrogenetic interpretations. *Lunar Sci. Conf. 6th Proc.* **6**, 921–944.
- Khan, A., Mosegaard, K., Rasmussen, K.L., 2000. A new seismic velocity model for the Moon from a Monte Carlo inversion of the Apollo lunar seismic data. *Geophys. Res. Lett.* **27**, 1591–1594.
- Kushiro, I., Ikeda, Y., Nakamura, Y., 1972. Petrology of Apollo 14 high-alumina basalt. *Lunar Sci. Conf. 3rd, Proc.* **3**, 115–129.
- Lindsley, D.H., 1980. Phase equilibria of pyroxenes at pressures >1 atmosphere. *Rev. Mineral.* **7**, 289–307.
- Lognonne, P., Gagnepain-Beyneix, J., Chenet, H., 2003. A new seismic model of the Moon: implications for structure, thermal evolution and formation of the Moon. *Earth Planet. Sci. Lett.* **211**, 27–44.
- Longhi, J., 1992a. Experimental petrology and petrogenesis of mare volcanics. *Geochim. Cosmochim. Acta* **56**, 2235–2251.
- Longhi, J., 1992b. Origin of picritic green glass magmas by polybaric fractional fusion. *Lunar Planet. Sci. Conf. 13th, Proc.* **22**, 343–353.
- Longhi, J., 1995. Liquidus equilibria of some primary lunar and terrestrial melts in the garnet stability field. *Geochim. Cosmochim. Acta* **59**, 2375–2386.
- Longhi, J., Walker, D., Grove, T.L., Stolper, E.M., Hays, J.F., 1974. The petrology of the Apollo 17 mare basalts. *Lunar Sci. Conf. 5th Proc.* **5**, 447–469.
- Neal, C.R., 2001. Interior of the Moon: the presence of garnet in the primitive deep lunar mantle. *J. Geophys. Res.* **106**, 27865–27885.
- Neal, C.R., Shearer, C.K., 2004. Garnet in the lunar mantle: further evidence from volcanic glasses. *Lunar Planet. Sci.* **XXXV**, 2135.
- Nicholls, I.A., Harris, K.L., 1980. Experimental rare earth element partition coefficients for garnet, clinopyroxene and amphibole coexisting with andesitic and basaltic liquids. *Geochim. Cosmochim. Acta* **44**, 287–308.
- O'Hara, M.J., Biggar, G.M., Richardson, S.W., Ford, E.C., Jamieson, B.G., 1970. The nature of seas, mascons and the lunar interior in the light of experimental studies. *Lunar Sci. Conf. 1st, Proc.*, 695–710.
- Ohtani, E., Kawabe, I., Moriyama, J., Nagata, Y., 1989. Partitioning of elements between majorite garnet and melt and implications for petrogenesis of komatiite. *Contrib. Mineral. Petrol.* **103**, 263–269.
- Onuma, N., Higuchi, H., Wakita, H., Nagasawa, H., 1968. Trace element partition between two pyroxenes and the host lava. *Earth Planet. Sci. Lett.* **5**, 47–51.
- Papike, J.J., Ryder, G., Shearer, C.K., 1998. Lunar samples. *Rev. Mineral.* **36** (1–5), 234.
- Pertermann, M., Hirschmann, M.M., Hametner, K., Gunther, D., Schmidt, M.W., 2004. Experimental determination of trace element partitioning between garnet and silica-rich liquid during anhydrous partial melting of eclogite. *Geochim. Geophys. Geosyst.* **5**, 2003GC000638.
- Ringwood, A.E., Essene, E., 1970. Petrogenesis of Apollo 11 basalts, internal constitution and origin of the Moon. *Lunar Sci. Conf. 1st, Proc.* **1**, 769–799.
- Salters, V.J.M., Hart, S.R., 1989. The hafnium paradox and the role of garnet in the source of mid-ocean-ridge basalts. *Nature* **342**, 420–422.
- Salters, V.J.M., Longhi, J., 1999. Trace element partitioning during the initial stages of melting beneath mid-ocean ridges. *Earth Planet. Sci. Lett.* **166**, 15–30.
- Salters, V.J.M., Longhi, J.E., Bizimis, M., 2002. Near mantle solidus trace element partitioning at pressures up to 3.4 GPa. *Geochim. Geophys. Geosyst.* **3**, 2001GC000148.
- Shannon, R.D., 1976. Revised effective ionic radii and systematic studies of interatomic distances in halides and chalcogenides. *Acta Crystallogr.* **A32**, 751–767.
- Shearer, C.K., Neal, C.R., Draper, D.S., Papike, J.J., Agee, C., 2003. Melting in the deep lunar mantle. *Lunar Planet. Sci.* **XXXIV**, 1456.
- Shearer, C.K., Papike, J.J., 1993. Basaltic magmatism on the Moon: a perspective from volcanic picritic glass beads. *Geochim. Cosmochim. Acta* **57**, 4785–4812.
- Shearer, C.K., Papike, J.J., 1999. Magmatic evolution of the Moon. *Am. Mineral.* **84**, 1469–1494.
- Steele, A.M., Colson, R.O., Korotev, R.L., Haskin, L.A., 1992. Apollo 15 green glass: compositional distribution and petrogenesis. *Geochim. Cosmochim. Acta* **56**, 4075–4090.
- Suzuki, T., Akaogi, M., Nakamura, E., 2000. Partitioning of major elements between garnet-structured minerals and silicate melt at pressure of 3–15 GPa. *Phys. Earth Planet. Interior.* **120**, 79–92.
- Taylor, S.R., 1982. *Planetary Science: A Lunar Perspective*. Lunar and Planetary Institute.
- Taylor, S.R., 1992. *Solar System Evolution: A New Perspective: An Inquiry into the Chemical Composition, Origin, and Evolution of the Solar System*. Cambridge University Press, Cambridge.
- Van Orman, J.A., Grove, T.L., 2000. Origin of lunar high-titanium ultramafic glasses; constraints from phase relations and dissolution kinetics of clinopyroxene-ilmenite cumulates. *Meteorit. Planet. Sci.* **35**, 783–794.
- van Westrenen, W., Blundy, J., Wood, B., 1999. Crystal-chemical controls on trace element partitioning between garnet and anhydrous silicate melt. *Am. Mineral.* **84**, 838–847.
- van Westrenen, W., Blundy, J.D., Wood, B.J., 2000. Effect of Fe<sup>2+</sup> on garnet-melt trace element partitioning: experiments in FCMAS and quantification of crystal-chemical controls in natural systems. *Lithos* **53**, 189–201.
- van Westrenen, W., Blundy, J.D., Wood, B.J., 2001a. High field strength element/rare earth element fractionation during partial melting in the presence of garnet: implications for identification of mantle heterogeneities. *Geochim. Geophys. Geosyst.* **2**, 2000GC000133.
- van Westrenen, W., Wood, B., Blundy, J., 2001b. A predictive thermodynamic model of garnet-melt trace element partitioning. *Contrib. Mineral. Petrol.* **142**, 219–234.
- Wagner, T.P., Grove, T.L., 1997. Experimental constraints on the origin of lunar high-Ti ultramafic glasses. *Geochim. Cosmochim. Acta* **61**, 1315–1327.
- Walker, D., Longhi, J., Hays, J.F., 1972. Experimental petrology and origin of Fra Mauro rocks and soil. *Lunar Sci. Conf. 3rd, Proc.* **88**, 770–772.
- Walker, D., Longhi, J., Hays, J.F., 1976. Heterogeneity in titaniferous lunar basalts. *Earth Planet. Sci. Lett.* **30**, 27–36.
- Walker, D., Longhi, J., Lasaga, A.C., Stolper, E.M., Grove, T.L., Hays, J.F., 1977. Slowly cooled microgabbros 15555 and 15065. *Lunar Sci. Conf. 8th, Proc.* **8**, 1524–1547.
- Walker, D., Longhi, J., Stolper, E.M., Grove, T.L., Hays, J.F., 1975. Origin of titaniferous lunar basalts. *Geochim. Cosmochim. Acta* **39**, 1219–1235.
- Xirouchakis, D., Draper, D.S., Agee, C.B., 2002. The garnet to majorite transformation in mafic compositions. *Lunar Planet. Sci.* **XXXII**, 1316.
- Yurimoto, H., Ohtani, E., 1992. Element partitioning between majorite and liquid: a secondary ion mass spectrometric study. *Geophys. Res. Lett.* **19**, 17–20.